ETD Archive

2011

Culture, Efficacy, and Outcome Expectancy in Teacher Preparation;How Do the Beliefs of Pre-Service Interns, Mentor Teachers, University Supervisors and Teacher Educators Compare?

Sashelle Thomas Alexander
Cleveland State University

ROTOR POSITION AND VIBRATION CONTROL

FOR AEROSPACE FLYWHEEL ENERGY STORAGE DEVICES AND OTHER

VIBRATION BASED DEVICES

B.X.S. ALEXANDER

Bachelor of Arts in Philosophy of Physics

Honors Tutorial College, Ohio University

June 2004

Master of Science in Electrical Engineering

Cleveland State University

August 2006

submitted in partial fulfillment of requirements for the degree

DOCTOR OF ENGINEERING in Electrical Engineering

at

CLEVELAND STATE UNIVERSITY

June, 2008

ACKNOWLEDGEMENTS

I would like to express my gratitude to Dr. Paul Lin and Dr. Lili Dong for their unwavering guidance, which has been the primary impetus behind the research.

I also want to thank the members of my dissertation committee, who have had the time and patience to supervise my projects.

Engineering is a noble endeavor, and coming from an arts and humanities background, I am grateful for having been given the chance to experience it first hand. I have developed great respect for this most selfless of disciplines.

ROTOR POSITION AND VIBRATION CONTROL

FOR AEROSPACE FLYWHEEL ENERGY STORAGE DEVICES AND OTHER

VIBRATION BASED DEVICES

B.X.S. ALEXANDER

ABSTRACT

Flywheel energy storage has distinct advantages over conventional energy storage methods such as electrochemical batteries. Because the energy density of a flywheel rotor increases quadratically with its speed, the foremost goal in flywheel design is to achieve sustainable high speeds of the rotor. Many issues exist with the flywheel rotor operation at high and varying speeds. A prominent problem is synchronous rotor vibration, which can drastically limit the sustainable rotor speed.

In a set of projects, the novel Active Disturbance Rejection Control (ADRC) is applied to various problems of flywheel rotor operation. These applications include rotor levitation, steady state rotation at high speeds and accelerating operation. Several models such as the lumped mass model and distributed three-mass models have been analyzed. In each of these applications, the ADRC has been extended to cope with disturbance, noise, and control effort optimization; it also has been compared to various industry-standard controllers such as PID and PD/observer, and is proven to be superior. The control

performance of the PID controller and the PD/observer currently used at NASA Glenn has been improved by as much as an order of magnitude.

Due to the universality of the second order system, the results obtained in the rotor vibration problem can be straightforwardly extended to other vibrational systems, particularly, the MEMS gyroscope. Potential uses of a new nonlinear controller, which inherits the ease of use of the traditional PID, are also discussed.

TABLE OF CONTENTS

LIST OF TABLES

LIST OF FIGURES

xi

CHAPTER I

INTRODUCTION

1.1   *Background*

The flywheel is a mechanical device which consists of a rotor, most commonly of cylindrical shape, that stores kinetic energy when set in motion. The flywheel's kinetic energy depends linearly on *I*, the moment of inertia of the rotor, and quadratically on the angular velocity of rotation, ω.

$$E_{kin} = \frac{1}{2} I \omega^2 \qquad (1.1)$$

A unique aspect is that the energy density (energy per unit mass) of the flywheel can be increased with increasing rotation speed. Equation (1.1) reveals that the energy density is solely dependent on angular velocity.

1

$$\frac{E}{m} \propto \omega^2 \qquad\qquad (1.2)$$

The mechanical nature of the flywheel energy storage has distinct advantages over conventional energy storage systems such as batteries. A prominent feature is ultra-fast power storage and release capabilities (pulsed applications). The energy content of the flywheel can be easily modified by regulating the rotor speed, as evident from equation (1.1). Through the use of modern power controls systems, this process has been very efficient and rapid. Charging is achievable in less than 15 minutes in high speed flywheels, and the round trip energy efficiency can be as high as 80%, if frictional losses are checked.

Unlike conventional batteries, the energy storage capability of flywheels is insensitive to variations in temperature and pressure, and the device itself has relatively long life times. This property has attracted applications in aerospace engineering, where a main concern is to develop devices with adequate energy density and long life times. The NASA Glenn Research Center (GRC) is currently developing high-speed flywheels for use on spacecraft, with the objective of doubling the life and payload capabilities of satellites 0. Since the energy density of a flywheel increases quadratically with its rotor speed, the foremost goal in flywheel design is to achieve sustainable high speed operation of the rotor. However, many factors can limit the achievable speed.

The material strength of the flywheel rotor predicts an upper limit on its speed, referred to as the burst speed. At this speed the material would disintegrate due to high centrifugal

forces. This theoretical limit is rarely achieved due to prominent rotor vibrations at critical speeds *below* the burst speed.

Reports from NASA Glenn Research Center 0, [4] suggest that rotor vibration is the practical limiting factor on rotor speeds. Rotor vibration manifests itself as the deviation of the rotor from its equilibrium position. Large amplitudes of vibration thus cause the rotor to significantly deviate from its equilibrium position and hit other objects in the air gap, causing catastrophic failure.

Aerospace flywheel rotor control requires adequate actuators. The most common choice is active magnetic bearing (AMB) because it allows no-contact actuation and has comparatively higher actuation speeds. The AMB works by generating magnetic forces on the rotor. This method has distinct advantages over other actuation methods, which will be discussed and evaluated in detail in Chapter II.

The rotor operation of aerospace flywheels can be characterized in terms of three distinct operational modes. Different physical models are used to describe each individual operational mode. Firstly, the rotor needs to be levitated into its equilibrium position when the flywheel rotor is not spinning. The physical model used to describe the levitation treats the flywheel rotor as a lumped mass. Secondly, the flywheel is spun up to its operating angular speed. During this process, the rotor undergoes accelerating angular motion. Afterward, the rotor enters steady state operation, where its angular speed is constant. In this research, all three modes of flywheel operation will be addressed.

Due to the complexity of the rotor vibration problem, most engineers have resorted to primitive control technologies such as the proportional-integral-derivative (PID) controller [5], which presently accounts for over 95% of all industrial control applications. This is not because practicing engineers are unaware of recently developed control methods, but because they find the advanced controllers difficult to tune and that it requires years of training. The aerospace group at NASA Glenn presently only uses PID controllers for exactly this reason. The overwhelming advantage in selecting PID over more advanced controllers is its ease of use, with only three tuning parameters and applicability to a vast range of plant models. It is very important to reduce the controller complexity whenever possible, and thus the overall complexity of the closed loop system.

1.2   Motivation

The overall objective of this research is to apply a practical control method to flywheel operations. This practical control method should improve on the PID in terms of performance, while retaining its simplicity of use with only a small number of tuning parameters. Such a control technique has been recently proposed and termed Active Disturbance Rejection Control (ADRC), which is based on the PD controller with a disturbance observer. The tuning parameters of both the controller and observer have been systematically parameterized so as to reduce the total number of tuning parameters to two.

1.3   ADRC as a Control Paradigm

In this section, the PID control scheme and the active disturbance rejection scheme are compared from a high-level perspective. A philosophical account of ADRC is presented, which lays out its fundamental ideas while only using rudimentary algebra. I hope that it would appeal to the general audience.

A PID controller monitors the output of the plant and compares it, in real time, to the desired set point to generate an error signal. When disturbance is present, it affects the plant output and leads to an increase in the error signal. The control law computes the control output based on this error signal, in an attempt to reject the disturbance by driving the error to zero. In each specific application, the PID controller can be tuned based on trial-and-error, a technique followed in most industrial applications. The controller has to be retuned for different plants. The small number of controller tuning parameters makes such a technique feasible.

PID control is an example of *Passive Disturbance Rejection* (PDR) control. The PDR functions by driving the difference between plant output and set point to zero, but does not do so by actively rejecting disturbances. There exists a distinct trade-off between the controller's ability to reject disturbance and to track the set point.

A controller's ability to reject disturbance can be drastically improved if the disturbance is estimated, and compensated for, in real time. Just like the feedback sensor that monitors the difference between the plant output and the desired set point, one can design

an observer to monitor the deviation of the actual plant dynamics from a desired nominal model. The difference can be cancelled out via the control input so to reduce the plant to a nominal plant. This is the idea behind the *Active Disturbance Rejection* (ADR) paradigm, on which ESO is based. This is the motivation behind my hypothesis that both PID and ESO are "error-based": in the case with ESO, the measured error is between the observed, real-time plant and the desired, nominal plant. The choice of the nominal plant is conditioned by the circumstances of the control design. Take a motion control problem for instance, which is governed by Newton's Law

$$F = m\ddot{x} \tag{1.3}$$

For control purposes, the forces affecting the position output x can be distinguished as

$$F_{internal} + F_{actuator} + F_{disturbance} = m\ddot{x} \tag{1.4}$$

The internal forces arise from the dynamics of the plant model. The actuator forces convey the control input, affecting the dynamics of the system. Both forces are thus given by the model and the control law and are assumed to be known. The disturbance force represents unknown external disturbances and plant variations not included in the model. Its real-time value can be estimated if the mass and the acceleration are known:

$$F_{disturbance} = m\ddot{x} - (F_{internal} + F_{actuator}) \tag{1.5}$$

Once estimated, the disturbance can be actively compensated for by incorporating it into the control law, such as

$$F_{actuator} = -F_{disturbance} \qquad (1.6)$$

This reduces the plant (1.4) to the nominal plant given by

$$F_{internal} = m\ddot{x} \qquad (1.7)$$

By choosing different control laws, equation (1.4) can be reduced to different nominal plants. One could even use the control law to cancel out the internal forces in addition to disturbance, which is what ESO amounts to. The ESO is designed such that all internal forces in (1.7) are reduced to a constant value.

Purged of unknown dynamics, nominal plants such as (1.7) can be now controlled with an additional PDR controller to achieve set point tracking. Since the previous disturbance cancellation has led to a high disturbance rejection capacity, the PDR controller can be tuned for tracking optimization. The combination of both active and passive disturbance rejection gives rise to a control strategy capable of both disturbance rejection and high performance set-point tracking. The recently proposed Active Disturbance Rejection Control (ADRC) is a practical implementation of this new paradigm. By targeting the issues of disturbance rejection and set point tracking successively and separately, one obtains a two-degrees-of-freedom control flow (Figure 36).
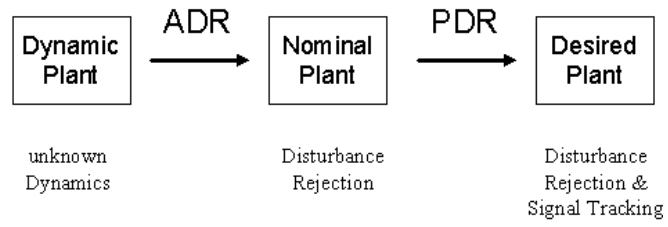
Figure 1: Two-degrees-of-freedom ADRC control flow, an illustration of the ADRC paradigm

This completes the analysis of the Active Disturbance Rejection Control.

CHAPTER II

DISCUSSION OF VARIOUS FLYWHEEL ROTOR CONTROL ACTUATORS

2.1   Literature Review

Vibration is a main problem in rotor dynamics, and most flywheel rotor actuators were designed with vibration control in mind. Rotor mass imbalance is the main cause of vibration, and it is an unavoidable result of imperfection in rotor manufacturing. The physical effect of imbalance can be compensated through force actuators which in a sense rebalance the rotor during operation. Various methodologies have been proposed to address the issue.

Vibration control devices can be roughly categorized as active and passive devices. Passive devices have been employed early on in rotating machinery design due to their simple operation. Examples are purely mechanical dampers based on flexible structures [6] or squeeze-film dampers [7]. More recently, advanced materials such as magnetorheological fluids [8] have also been proposed. Passive magnetic bearings have

been researched at NASA Glenn [9]. All such devices rely on the presence of a medium surrounding the rotor surface which exerts a constant frictional force on the rotor. Passive devices cannot be adjusted during operation; thus the actuation force is not variable. Moreover, overall energy losses are considerable in such damped systems. For this reason, passive devices are rarely used for flywheel energy storage; the energy losses would de facto defy the purpose of energy storage.

By contrast, active devices can be adjusted during operation according to the vibration characteristic. This allows for closed loop control. Active vibration control devices are far more efficient in terms of energy consumption, and far more effective. Almost all vibration control devices for flywheel energy storage are active devices. There are three main types of active vibration control devices used today: mass redistribution actuators, piezoelectric actuators, and active magnetic bearings (AMB).

2.2   Mass Redistributors

Mass redistribution actuators are mounted on the rotor and allow for the center of mass of the rotor to be changed. The vibration of the rotating machinery is directly suppressed by canceling out the rotor imbalance, and the associated centrifugal force. In order for this method to work, the imbalance has to be estimated. This can be achieved through measuring the vibrations at very low speed. A schematic drawing of a mass-redistribution actuator is shown in Figure 2, demonstrating the movable ring structure used to achieve mass redistribution. Such a device has been successfully implemented in a closed loop configuration by Dyer [10].
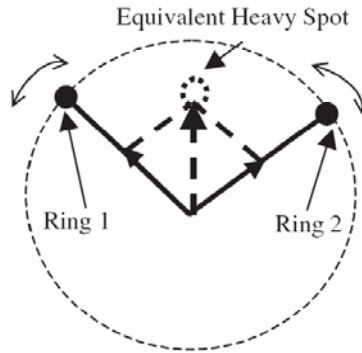
Figure 2: Mass redistribution actuator

The first implemented mass redistributor was based on the motion of correction masses along two perpendicular axes fixed to the rotating system [10]. The masses are driven by two small servomotors, and the power for the motors was supplied by slip rings. The only input to the active balancing system is the vibration measurement. Subsequent studies [12], [13] found that if the rotating frequency is close to the resonant frequency of the system, errors in measurement can lead to serious errors in the closed loop system. The performance inaccuracy of mass redistribution devices has been often criticized [14], and remains one of the unresolved issues in this application: Due to the use of small servomotors to drive the correcting masses, the actuation speed of the device is low. Flywheel rotors operating at high steady state speeds do not require large actuation force, but actuation speed is *essential*. Mass redistribution actuator will thus not suffice for high speed operations.

2.3 Piezoelectric Actuators

Piezoelectric actuators are a new type of force actuator which operates through voltage induced deformation of material. This is known as the piezoelectric effect [15]. Such

11

actuators are small patches attached to the rotor [16], [17]. Due to the nature of the piezoelectric effect, such devices are capable of fast dynamic response in force actuation. Another significant advantage is high stiffness and accuracy [18], [19]. For instance, in a recent study [20], Lead Zirconate Titanate [21] patches are surface-bounded on the rotor shaft surface (Figure 3).
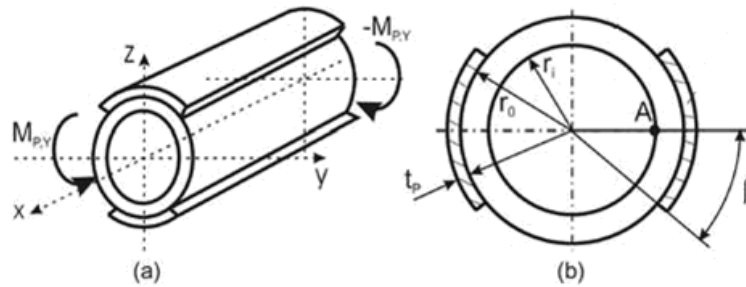
Figure 3: Piezoelectric (PZT) patches on rotor shaft surface

The major disadvantage of piezoelectric actuators is the low actuation force deliverable due to the small size of the patches. Such small forces are insufficient for high-speed flywheel operations. Larger patch sizes constitute a problem in manufacturing.

2.4   Active Magnetic Bearing

Currently, the most widely employed rotor vibration control device is the active magnetic bearing (AMB) [24], which creates magnetostatic forces on the rotor, and is thus a non-contact actuator, offering advantages such as reduced frictional losses and reduced mechanical wear and tear. Because of its importance in closed loop control systems, we shall give a more detailed account of the AMB vibration control system. When used with a power amplifier, the AMB is capable of delivering relatively large actuation forces.

The schematic arrangement of pairs of AMBs for rotor vibration control is shown in Figure 4; only the AMB pair in one dimension is shown. In practice at least two pairs are needed to control the vibrations, since the vibration orbit of the rotor is circular. The magnetic forces on the rotor are induced by a ferromagnetic sheet on the surface of the rotor.
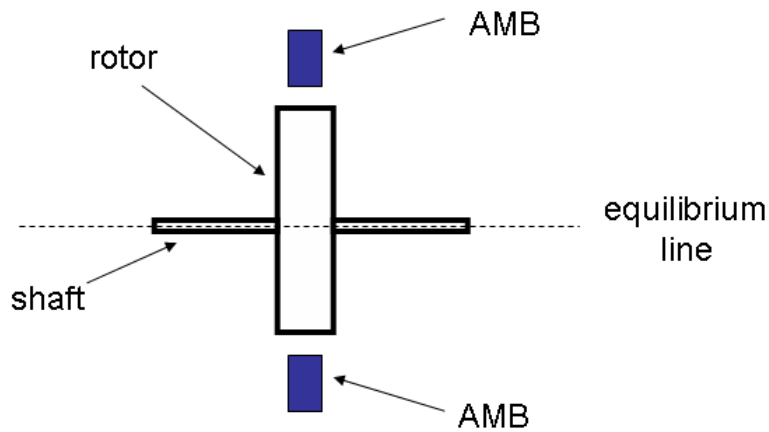
Figure 4: Schematic AMB configuration of rotor vibration control

The active magnetic bearing is constructed using electro-magnets, and the output flux can be controlled by varying the voltage or current in the magnet coils, via Ampere's law [27]. Figure 5 shows a schematic representation of AMB force actuation. The design in Figure 4 also provides additional robustness protection in the face of external disturbances.
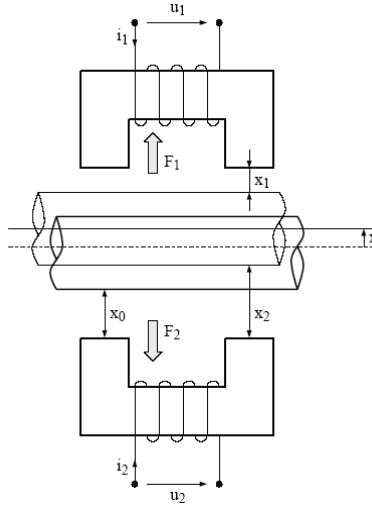
Figure 5: An example of AMB force actuation

2.5   Load and Frequency Limitations of AMB

The operation of AMBs for rotor control is characterized by how much force the magnets can generate and how fast the forces can be generated. The amount of deliverable force is termed load, and how fast the forces are generated is described in terms of power bandwidth. These two qualities are fundamental in rotor control, especially when vibrations are present, since the load and bandwidth of the AMB limit the achievable speed of the rotor.

The maximum load, f_{max}, is physically dictated by the saturation properties of the magnets. This is because the amount of flux the magnets can generate cannot grow infinite, and thus there is always an upper limit to the force the magnet can deliver. Any overload beyond this maximum load will cause the rotor to break away from the equilibrium position and crash against the bearing. The maximum load depends on the geometrical properties of the bearing magnets, such as size. The maximum load is

14

inversely proportional to the bearing diameter and bearing width. It has been estimated [24] that for radial magnetic bearings (with conventional ferromagnetic coating of the rotor), the following relationship holds:

$$\frac{f_{max}}{d \cdot b} = 32(\frac{N}{cm^2}) \qquad (2.1)$$

Where d denotes the bearing diameter, and b denotes the bearing width of the magnetically active part. The quantity on the left hand side of the equation is called specific load. The value of 32 N/cm^2 is four times lower than that for oil lubricated bearing, a passive vibration control device discussed at the beginning of this chapter. The relationship (2.1) also shows that in order to increase the maximum achievable load, the dimensions of the bearing have to be increased, according to Figure 6. The range of f_{max} is thus in the kilo Newtons range.
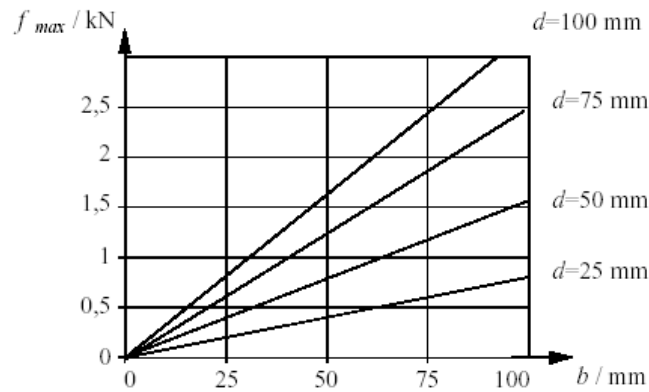
Figure 6: Dependence of maximum achievable load on bearing dimensions

The power bandwidth ω_{pbw} is essentially the highest frequency at which the actuator magnets can still operate. The power bandwidth can be improved with a higher output power amplifier. The power bandwidth also depends on the air gap and maximum load according to the following relationship [24]:

$$\omega_{pbw} = 0.92 \frac{P_{max}}{s_0 f_{max}} \tag{2.2}$$

Where P_{max} is the output of the power amplifier and s_0 is the air gap distance. From this relationship, a force of 1000N can be generated with a 1kW amplifier in an air gap of 1mm only with a frequency of 920 rad/s. This value, as we shall see in the chapter on vibration control, is sufficient for rotor control at a speed below 10,000 RPM. Obviously, the power bandwidth can be increased with a smaller air gap. Most air gap distances range from 0.1 to 0.7 mm.

CHAPTER III

ROTOR LEVITATION CONTROL

3.1   *Problem Formulation*

The object of rotor levitation control is to move the rotor from its initial position (where

the rotor is situated when not in operation) up to its equilibrium position (where the rotor

then can be spun to its operating speed). AMB is used in general to achieve this

levitation. In this control problem, the initial rotor position may be taken as zero, while

the equilibrium position is the air gap distance (the distance between the rotor and the

bearing). The rotor is physically described as a point mass, and the model leads to a

second order transfer function with an unstable pole. This simple model is also often used

to study the effect of external disturbances on the rotor [25], and the related disturbance

rejection control issues.

The levitation problem has been well addressed in literature, as various experimental and model setups have been studied. Hubbard [31] used linear-quadratic design in their pendulous supported flywheel. Stanway [32] used eigenstructure assignment for the control of suspension systems for rotating machinery within a magnetic field. Sinha [33] considered sliding mode control of a rigid motor via magnetic bearings. Salm [34] demonstrated modal control of a flexible rotor. Matsumura [35] used an integral type servo-controlled design via solution of a linear quadratic regulator problem, for a horizontal rotor-magnetic-bearing system, and Hung [36] considered magnetic bearing control using fuzzy logic. These proposed controllers are often of such great complexity that they have become highly impractical. Most of the aforementioned controllers have never been implemented in industry because of the tuning effort associated with the application of the controller. As a result, the PID controller, benefiting from its ease of use, is by still far the most prevalent, and cost-effective controller used for active magnetic bearing control.

The flywheel group at GRC has recently implemented a PD controller with a velocity observer for the levitation problem [4]. The goal of this chapter is to apply a PD controller with a disturbance observer for better performance. The latter control strategy is also known as active disturbance rejection control (ADRC). A systematic parameterization strategy is introduced aimed at reducing the tuning effort of the user. Finally, the two control strategies will be compared and evaluated in simulation both in terms of performance as well as control effort.

3.2   Physical Model

The position transfer function of the rotor can be obtained by mechanical modeling of the electromechanical components. The rotor of mass *m* is assumed to be rigid. Then the plant can be represented by a mass-spring system. The corresponding force diagram, drawn by Dever [4], for a rigid body in a magnetic bearing system is shown in Figure 7.
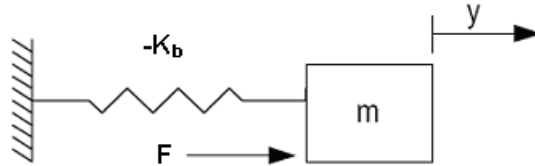
Figure 7: Force diagram for rotor position model

The position of the rotor, *y*, can be controlled through the actuator force, *F*, which is generated via the electromagnets. The functional relationship between magnetic coil current and output magnetic force is normally known with relative high accuracy. Therefore, in designing the control law, one may treat the actuator force as the control signal. In actual implementation, the control force can be easily converted into a control current signal.

From Figure 7, the differential equation for rotor dynamics can be derived,

$$m\ddot{y} - K_b y = F \tag{3.1}$$

where *m* is the mass of the rotor, and K_b is the experimentally determined stiffness constant (its negative sign is due to the fact that the force from the bearing is attractive).

By taking the Laplace transform of (3.1), one can obtain the open-loop position transfer function,

$$P(s) \equiv \frac{Y(s)}{F(s)} = \frac{1}{ms^2 - K_b}$$

(3.2)

which has poles at $\pm\sqrt{K_b/m}$. The presence of one of the poles in the right half plane makes the system unstable. Hence closed-loop control must be applied to stabilize it.

The physical significance of closed loop control is to allow the magnetic bearing to have a positive, variable stiffness, in lieu of the negative stiffness. In addition, since the system given by equation (3.2) does not contain a damping term, the closed-loop should ideally provide a variable damping force.

3.3   PD Controller Design

NASA Glenn's flywheel module High Speed Shaft (HSS) was originally implemented using only a proportional-derivative (PD) controller, which successfully levitated the flywheel shaft [4]. From a theoretical perspective, the PD controller provides the system with positive stiffness and damping. The PD-Controller Transfer function is given by,

$$C_{PD}(s) = k_p + k_d s$$

(3.3)

so that the closed-loop transfer function becomes

$$G_{cl} = \frac{C_{PD}P}{1 + C_{PD}P} = \frac{k_d}{m} \left[\frac{s + \dfrac{k_p}{k_d}}{s^2 + \dfrac{k_d}{m}s + \dfrac{k_p - K_b}{m}} \right]$$

(3.4)

20

Equation (3.4) reveals that the closed-loop system has the form of a mass-spring-damper system. The damping term can be regulated by the derivative parameter k_d. The poles of this system can be conveniently placed in the left half-plane by tuning both k_d and k_p. The value of the proportional gain k_p should be chosen to be larger than the stiffness constant K_b.

The PD controller suffers from a major drawback. Noise present in the output position sensor signal is increased by the use of the derivative term, which can substantially degrade the control quality. In response, the control signal can also become extremely noisy, leading to unnecessary control energy expenditure. Even though low pass filtering can be added to the sensor signals in an attempt to palliate high frequency noise; the filtering also adds phase lag to the system.

To address this issue, an observer was added, which estimates the velocity of the rotor and thus generates the feedback signal needed for damping control [4]. The observer employed is a classical state observer, whose inputs are a) position error and b) the control signal. The output of the observer is the estimated radial velocity of the rotor. In order for the observer's velocity estimation to converge to the actual value of the velocity, the observer has to be tuned adequately.

3.4   State Observer Design – Observer Gain Parameterization

In this section, the velocity observer is developed with a systematic parameterization, which reduces the number of observer tuning parameters to one. This would provide a drastic simplification in tuning effort. It also allows us to later better compare the velocity

observer to the disturbance observer, which also uses the parameterization technique for control effort reduction as part of the ADRC.

First a state space model of the plant is to be developed. The second order differential equation (3.1) can be rendered into two first order differential equations, by defining,

$$
\begin{aligned}
x_1 &= y \\
x_2 &= \dot{y}
\end{aligned}
\tag{3.5}
$$

so that (3.1) can be now written as

$$
\begin{aligned}
\dot{x}_1 &= x_2 \\
\dot{x}_2 &= \frac{K_b}{m} x_1 + \frac{F}{m}
\end{aligned}
\tag{3.6}
$$

Equation (3.6) can be represented in matrix notation,

$$
\begin{bmatrix} \dot{x}_1 \\ \dot{x}_2 \end{bmatrix} = \begin{bmatrix} 0 & 1 \\ K_b/m & 0 \end{bmatrix} \begin{bmatrix} x_1 \\ x_2 \end{bmatrix} + F \begin{bmatrix} 0 \\ 1/m \end{bmatrix}
\tag{3.7}
$$

which describes the dynamics of the state-vector x. The output of the system, usually denoted by y, is the position x_1. The relationship between the output and state-vector can be described by the following matrix multiplication

$$
y = \begin{bmatrix} 1 & 0 \end{bmatrix} \begin{bmatrix} x_1 \\ x_2 \end{bmatrix}
\tag{3.8}
$$

Thus for any given second order linear plant, the canonical plant model is given by a set of two equations:

$$\dot{x} = Ax + Bu$$
$$y = Cx \tag{3.9}$$

where A and B are the 2x2 matrix and 2x1 column vector, respectively, in equation (3.7), and C is the 1x2 row vector in (3.8). The control input, u, is the actuation force F.

The state space model of the observer is given by,

$$\dot{\hat{x}} = A\hat{x} + Bu + L(y - \hat{y})$$
$$\hat{y} = C\hat{x} \tag{3.10}$$

where variables representing the estimated values of the states are denoted by a hat above the symbols. The observer gain vector, L, is chosen in such a way to guarantee the convergence of the $y - \hat{y}$ error term to zero. The performance of the observer hinges on the choice of the observer gain vector. Substituting the second equation in (3.10) into the first one,

$$\dot{\hat{x}} = A\hat{x} + Bu + Ly - LC\hat{x}$$
$$= (A - LC)\hat{x} + Bu + Ly \tag{3.11}$$

the stability criterion translates into the requirement that the eigenvalues of the matrix $A - LC$ are in the left half-plane. This put a restriction on the choice of the elements of the gain vector L.

As an attempt to reduce tuning effort, the observer gains may be parameterized so that the eigenvalues of the $A - LC$ matrix are placed at the same location. This parameterization technique was developed by Gao [37], to reduce the tuning effort associated with ADRC. The parameterization is in terms of the elements of the control gain matrix,

23

$$L = \begin{bmatrix} \beta_1 & \beta_2 \end{bmatrix}^T \tag{3.12}$$

Using (3.12), and the expressions of the A and C matrix from (3.7) and (3.8), we can

write out explicitly the matrix $A - LC$:

$$A - LC = \begin{bmatrix} -\beta_1 & 1 \\ -\beta_2 + K_b/m & 0 \end{bmatrix} \tag{3.13}$$

The eigenvalues of $A - LC$ are obtained as

$$\det |A - LC - sI| = s^2 + \beta_1 s + (\beta_2 - K_b/m) \tag{3.14}$$

Gao's observer gain parameterization technique suggests to place the eigenvalues of

(3.14) at the same pole location in the left half plane, that is,

$$\det |A - LC - sI| = (s + \omega_O)^2 = s^2 + 2\omega_O s + \omega_O^2 \tag{3.15}$$

The pole location, ω_O, is referred to as the observer gain. Equating the right hand side of

(3.14) and (3.15), we obtain a parameterization of the observer gains in terms of the

observer bandwidth:

$$\begin{aligned} \beta_1 &= 2\omega_O \\ \beta_2 &= K_b/m + \omega_O^2 \end{aligned} \tag{3.16}$$

This parameterization procedure effectively reduces the number of observer tuning

parameter from two down to one. To implement the observer in Matlab Simulink for

simulation of closed loop control, the observer matrixes elements are parameterized

explicitly:

$$A - LC = \begin{bmatrix} -2\omega_O & 1 \\ -\omega_O^2 & 0 \end{bmatrix} \tag{3.17}$$

$$[B \vdots L] = \begin{bmatrix} 0 & 2\omega_O \\ 1/m & K_b/m + \omega_O^2 \end{bmatrix} \tag{3.18}$$

With the observer properly designed, we can use the estimated position and velocity values for the PD controller. The resulting control law is given by,

$$u = k_p (r - \hat{x}_1) + k_d (\dot{r} - \hat{x}_2). \tag{3.19}$$

3.5 *Active Disturbance Rejection*

As experienced by Dever and Jansen in their HSS module observer implementation [4], the observer gains are difficult to tune due to their sensitivity to variations in plant parameters. The fact is that during the operation of the flywheel, the measured parameter values of the plant may change due to vibration, friction, coil resistance changes. There exist a slew of unpredictable sources of uncertainty during actual control implementation. The classical Luenberger observer (3.10) is sensitive to changes in plant parameters because they affect the observer matrix elements.

It would be highly desirable to design an observer that can actually "detect" changes in the plant parameters and compensate for them. In particular, such an observer could be used to compensate for any real-time variations of the plant with respect to a desired nominal model plant. This would reduce the dependence of the observer/controller on the parameters of the plant. These are the essential ideas behind Active Disturbance Rejection Control (ADRC), for which such an observer was originally developed [38].

This observer is called an Extended State Observer (ESO), because its output includes all the states of the plant, and an extra state which measures the deviation of the plant from a given nominal plant. The ESO is a disturbance observer. In the following, the notions of the extra state and the nominal plant are explained in detail, as well as how they are used in ADRC's framework. The mathematical development of the ESO then follows, where the observer gain parameterization technique introduced in the last section will be used. The complete ADRC control law will also be presented.

3.6   Extended State Observer

In the broadest sense, an observer is an estimator whose outputs are the states of the plant, and whose inputs are the input and output of the plant. The classical Luenberger observer only estimates the states which were defined as the states of the plant (e.g. equation (3.5)). However much more information of the plant can be extracted based on the knowledge of its input and output. The key idea of ESO deals with how to extract valuable information by going beyond the original states of the plant. The following mathematical development applies to any second-order plant, whether linear or non-linear. It can be generalized to systems of any arbitrary order.

As an example, consider the second order plant (3.1) which can be rendered in the following general form,

$$\ddot{x} = f(\dot{x},t) + bu ,$$
(3.20)

where the variable x denotes the output of the plant (rotor position), and u denotes the control input of the plant (the external force F). The control input gain, b, can be

26

identified as $b = 1/m$ from equation (3.1). The function $f(\dot{x}, t)$ represents all the remaining terms in the differential equation. This term includes most of the information about the plant. It even captures possible time variation in plant parameters and may also include external disturbance. Gao [37] referred to this term as the generalized disturbance. If the generalized disturbance was absent, the plant (3.20) would simply reduce to a double integrator plant, $\ddot{x} = bu$. The goal of ESO design is to estimate the generalized disturbance, and to compensate for it in real-time, so that the system is forced to be like a double integral plant.

The key to ESO design is to make the generalized disturbance an additional state. For a second order system, the number of states would now increase from two to three. And the states variables for the ESO can be chosen as follows:

$$
\begin{aligned}
x_1 &= x \\
x_2 &= \dot{x} \\
x_3 &= f
\end{aligned}
\tag{3.21}
$$

The inclusion of f as an augmented third state is what motivated the term *extended state*. The extended state representation of the system dynamics can be derived directly from (3.20),

$$
\begin{aligned}
\dot{x}_1 &= x_2 \\
\dot{x}_2 &= x_3 + b_0 u \\
\dot{x}_3 &= h \\
y &= x_1
\end{aligned}
\tag{3.22}
$$

where h is the time derivative of f. The corresponding state space model is

$$\dot{x} = Ax + Bu + Eh$$
$$y = Cx$$

<div align="right">(3.23)</div>

where the matrixes are

$$A = \begin{bmatrix} 0 & 1 & 0 \\ 0 & 0 & 1 \\ 0 & 0 & 0 \end{bmatrix} \quad B = \begin{bmatrix} 0 \\ b_0 \\ 0 \end{bmatrix} \quad C = \begin{bmatrix} 1 \\ 0 \\ 0 \end{bmatrix}^T \quad E = \begin{bmatrix} 0 \\ 0 \\ 1 \end{bmatrix}$$

<div align="right">(3.24)</div>

Now the ESO can be constructed in analogy to the classical Luenberger observer (see equation (3.10)) :

$$\dot{\hat{x}} = A\hat{x} + Bu + Ly - LC\hat{x}$$
$$= (A - LC)\hat{x} + Bu + Ly$$

<div align="right">(3.25)</div>

The output states of this observer correspond to the estimated values of the quantities,

$$\hat{x}_1 \rightarrow x$$
$$\hat{x}_2 \rightarrow \dot{x}$$
$$\hat{x}_3 \rightarrow f$$

<div align="right">(3.26)</div>

and the observer gain vector L can be denoted as

$$L = \begin{bmatrix} \beta_1 & \beta_2 & \beta_3 \end{bmatrix}^T$$

<div align="right">(3.27)</div>

Now the observer gains can be computed following the parameterization technique introduced earlier (see (3.15)), by requiring all eigenvalues of the matrix A-LC to be placed at the pole w_o

$$\det|A - LC - sI| = (s + w_o)^3 = s^3 + 3w_o s^2 + 3w_o^2 s + w_o^3$$

<div align="right">(3.28)</div>

28

And the results become:

$$\beta_1 = 3w_0 \quad \beta_2 = 3w_0^2 \quad \beta_3 = w_0^3 \qquad (3.29)$$

Substituting (3.29) into (3.27), one obtains

$$\mathbf{A - LC} = \begin{bmatrix} -3w_0 & 1 & 0 \\ -3w_0^2 & 0 & 1 \\ -w_0^3 & 0 & 0 \end{bmatrix}, \quad \mathbf{B} = \begin{bmatrix} 0 \\ b_0 \\ 0 \end{bmatrix}, \quad \mathbf{L} = \begin{bmatrix} 3w_0 \\ 3w_0^2 \\ w_0^3 \end{bmatrix} \qquad (3.30)$$

As mentioned before, the classical Luenberger observer requires detailed knowledge of the plant, determined by the matrices *A* and *B*, is required for the determination of the observer gains. Yet in the extended state representation, the *A* and *B* matrices are constants. This feature enables one to choose the observer gains without detailed knowledge of the plant. This also is one of the reasons, as we shall see later, why the ADRC is less sensitive to variations in plant parameter. This can be a huge advantage in controller tuning.

With the extended state observer properly designed, the generalized disturbance can be compensated for. Assuming accurate estimation of *f* and *b*, that is

$$\hat{x}_3 \approx f \\ b_0 \approx b \qquad (3.31)$$

the compensated plant will be a double integral plant, which is then controlled using a PD controller. The resulting ADRC control law is

$$u = (-\hat{x}_3 + u_0)/b_0 \quad, \tag{3.32}$$

where the term $-\hat{x}_3$ compensates for the generalized disturbance. The term u_0 is the PD control law and is given by

$$u_0 = k_p(r - \hat{x}_1) + k_d(\dot{r} - \hat{x}_2), \tag{3.33}$$

where r is the setpoint. Gao [37] developed a systematic method to select the PD controller gains, so to attain critical damping. The idea here is to parameterize both controller gains in terms of a single tuning parameter, w_c, the controller bandwidth:

$$k_p = w_c^2 \qquad k_d = 2w_c \quad. \tag{3.34}$$

The parameterization scheme is motivated by the following ideas. Assuming proper cancellation of generalized disturbance, the double integrator plant is given by

$$\ddot{y} = u_0 \tag{3.35}$$

While assuming that the estimated values are accurate, we have,

$$\ddot{y} = k_p(r - y) - k_d\dot{y} \tag{3.36}$$

The closed-loop transfer function is thus given by

$$\frac{Y(s)}{R(s)} = \frac{k_p}{s^2 + k_d s + k_p} \tag{3.37}$$

where $Y(s)$ is the Laplace transform of y and $R(s)$ is the Laplace transform of r. With the choice of controller gains given by (3.34), the closed-loop transfer function achieves critical damping:

$$\frac{Y(s)}{R(s)} = \frac{w_c^2}{(s+w_c)^2} \qquad (3.38)$$

The ADRC control law (3.32) can be given in terms of the PD tuning parameters,

$$u = \frac{1}{b_0}\left[k_p(r-\hat{x}_1)+k_d(\dot{r}-\hat{x}_2)-\hat{x}_3\right], \qquad (3.39)$$

Because the ESO is a linear observer, it can be properly referred to as *Linear* Extended State Observer (LESO) to distinguish it from Han's original, non-linear ESO design [38]. And the resulting linear ADRC is hence referred to as LADRC. A Simulink implementation of LADRC to a second order plant is shown in Figure 8.
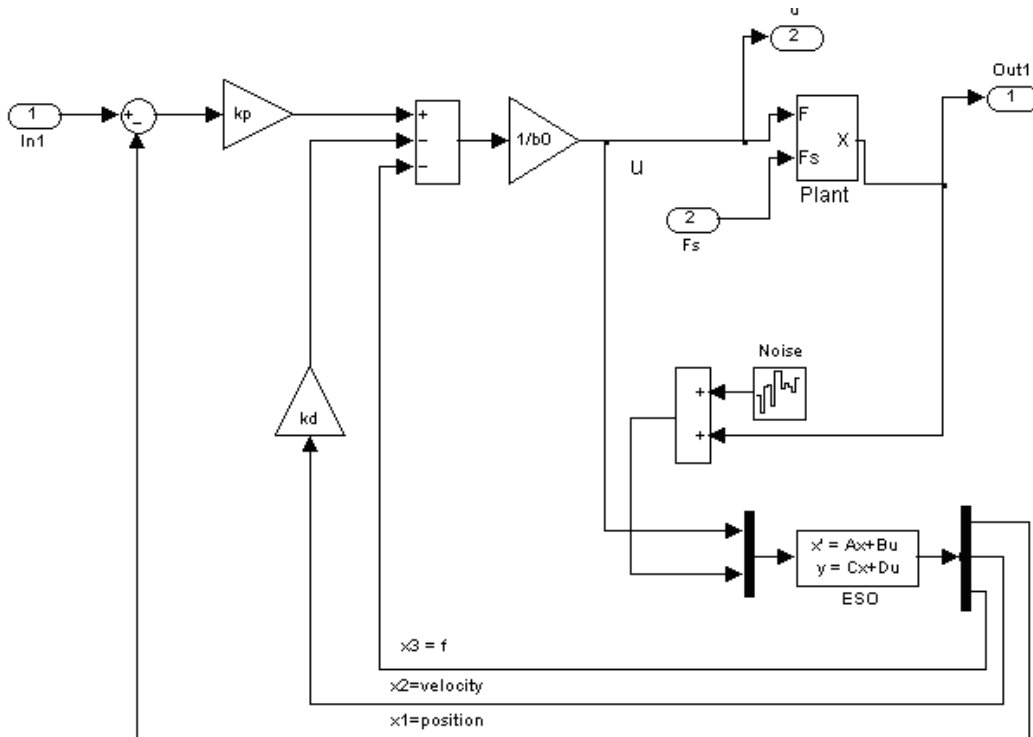

Figure 8: Simulink block diagram of ADRC for a second order plant

3.7   Comparison of Magnetic Bearing Plant Control

The LADRC magnetic bearing control is compared to PD/observer in simulation (Matlab Simulink 7.0.4). The PD/observer is a PD controller which uses a velocity observer. The mass m of the flywheel rotor is chosen as 1kg. The stiffness is $K_b = 0.4$ N/m. This choice of parameters renders the open loop plant transfer function (3.2) to be:

$$P(s) = \frac{Y(s)}{F(s)} = \frac{1}{s^2 - 0.4} \qquad (3.40)$$

The bandwidth of the plant can be determined from the Bode amplitude of (3.40), or from the equation $20\log|P(jw)| = $ -3dB. The value is approximately w_n=1.08rad/s.   The LADRC and PD/observer are implemented with the same controller bandwidth (w_c) and observer bandwidths (w_o), for a fair comparison of the two control techniques. The controllers are tested under three different scenarios. First, the levitation performance and the control efforts of both controllers are compared. Second, the disturbance rejection capabilities of both controllers are tested.

3.8   Levitation

The initial resting position of the rotor is taken as $x_0 = 0$, whereas the final position is $x_f = $ 1mm. This distance corresponds to the order of magnitude of the air gap between flywheel rotor and stator. Even though a step input of amplitude x_f would be sufficient for this application, the trapezoidal velocity profile is used instead, which avoids a large initial spike in control effort associated with the abrupt change of a step input. For the trapezoidal velocity profile, the shape of the input is designed so to make its derivative

shaped like a trapezoid. When integrated, this motion profile gives rise to a position input which settles to a steady state after a given period of time and is much smoother than the step input (see the upper graph in Figure 9). The trapezoidal velocity profile was created in such a way that the position input reaches a steady state of $x_f = 1mm$ in 0.3 seconds.

For the simulation with the trapezoidal velocity profile, the control parameters are chosen as follows. The observer bandwidths of both controller are placed at $w_o = 2000$, whereas the PD gains are both $w_c = 400$. This choice of the bandwidth is given by the rule of thumb $w_o \approx 5 \, w_c$, as proposed by [37]. With both controllers having identical tuning parameters, their performance and control effort are compared.
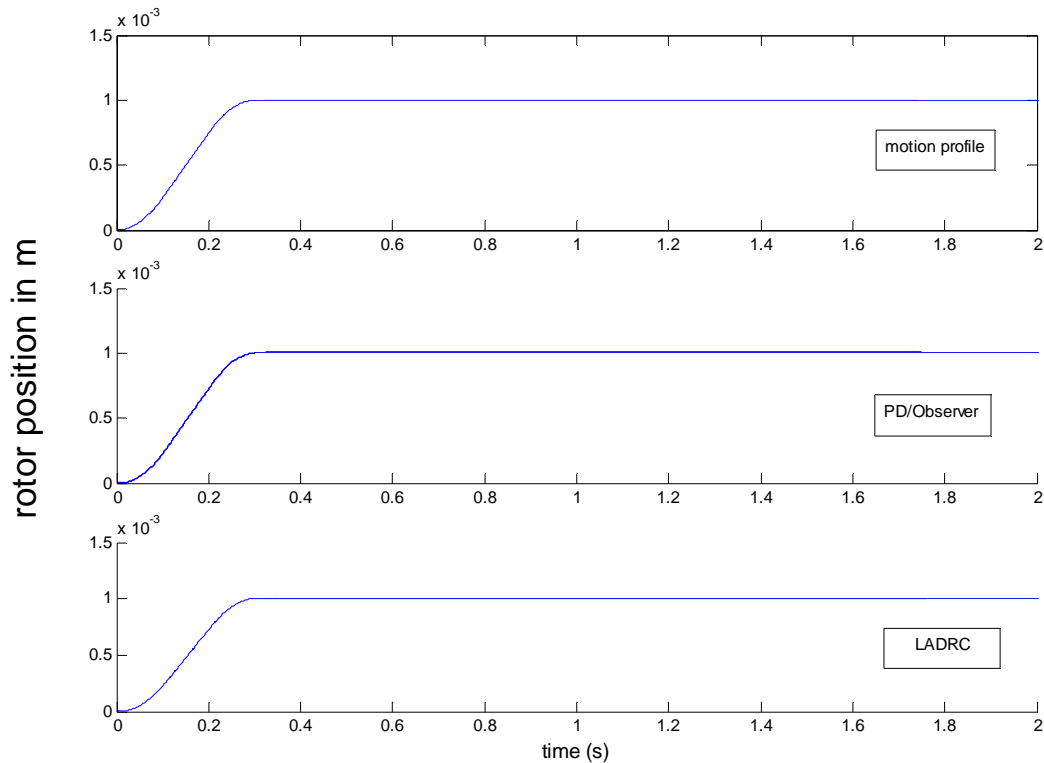
Figure 9: Performance comparison (noise-free)

Figure 9 and Figure 10 show the tracking performance and control effort without considering the noise effect. Both controllers exhibit virtually identical behavior, in both comparisons. In terms of control effort, the controllers show maximum amplitudes reaching just below 0.05 N, as well as constant zero steady state output.
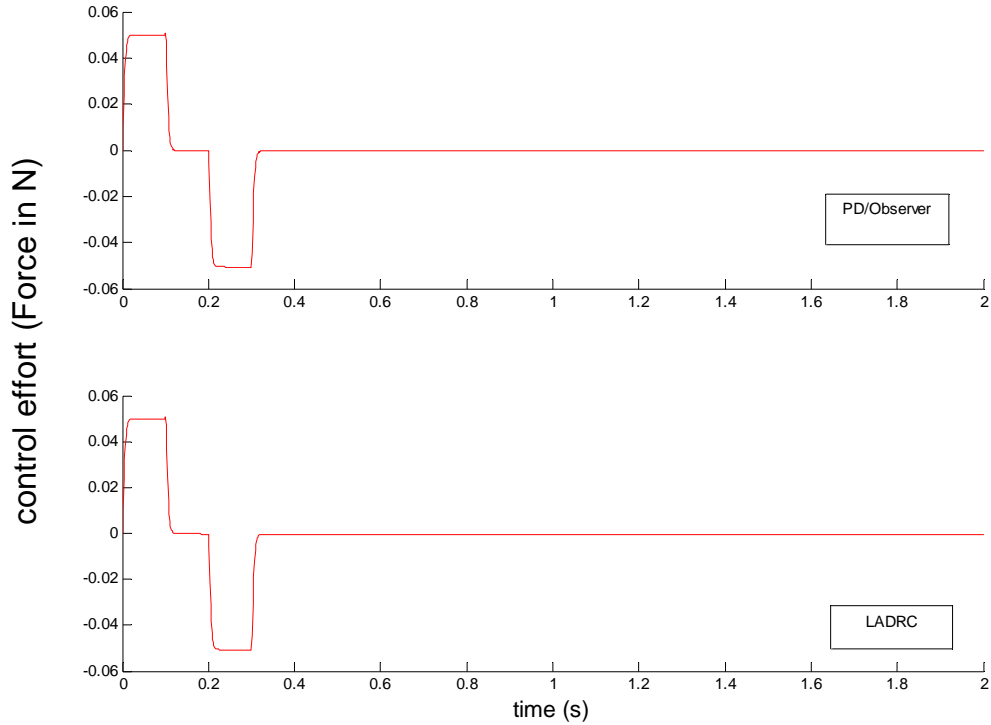
Figure 10: Control effort comparison (noise-free)

3.9   Constant Force Disturbance

Like most industrial devices, aerospace flywheels may be subject to external disturbance forces. The simplest case is the force of gravity on earth, which is often considered a constant disturbance force. In a space environment, the flywheel module will be subject to terrestrial or lunar gravitational fields. Because the orientation of the module in the space environment may not remain the same, the gravitational force rotor experiences

will be varying disturbance forces. From a controls perspective, the PD controller cannot reject disturbance without steady state error. PID controllers (with an additional integral term) are occasionally used, but the integral term adds phase lag to the controller. In NASA's and many other flywheel designs, disturbance forces are dealt with additional pairs of passive magnetic bearings, which cannot be controlled and add weight to the module. The ADRC however has intrinsic disturbance rejection properties and does not suffer from phase lag due to the integral term. The disturbance rejection properties are demonstrated in simulation. Figure 11 shows the controller performance under a constant step disturbance of -10 Newtons which is injected into the plant at t = 1s. The tuning parameters are the same as used in other simulations (w_o = 2000, w_c = 400).
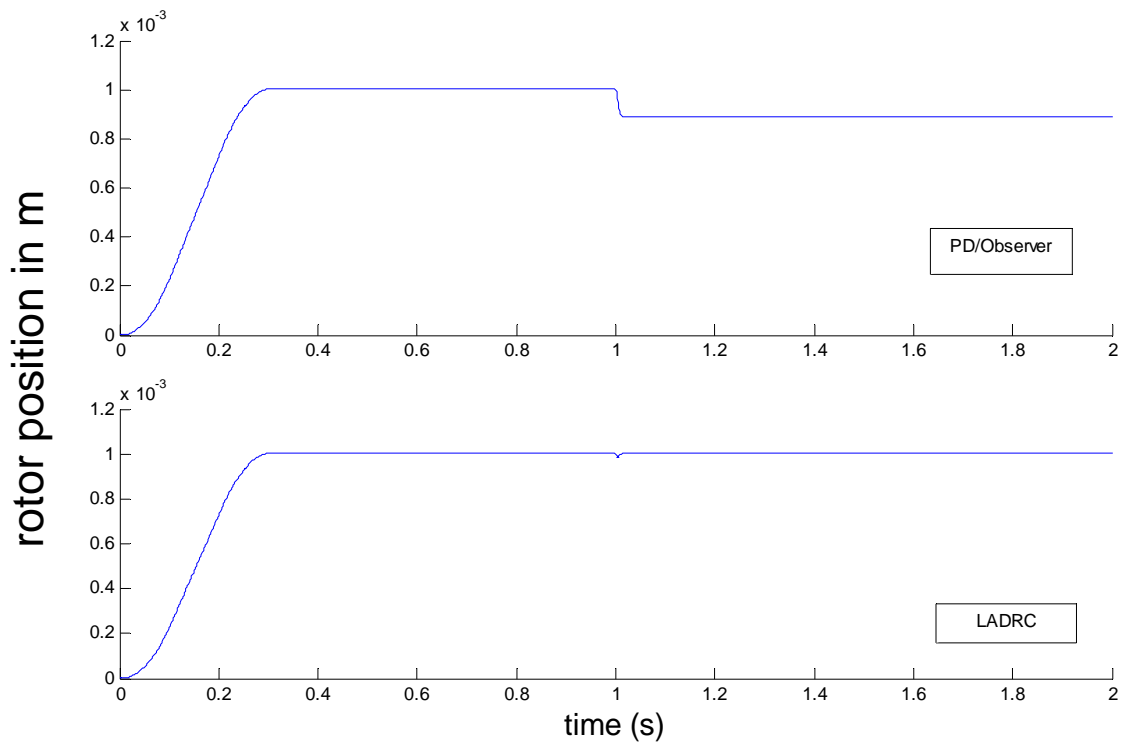

Figure 11: Performance comparison under constant force disturbance

As expected, the PD/observer controller exhibits a steady state error of approximately 0.1mm, whereas the LADRC only shows a transient minor dip in rotor position (less than 0.01 mm) recovers fully from the disturbance with no steady state error. Note also that there is no delay in tracking performance with LADRC, since the graphs show the transient behavior of both controllers to be the same.

In summary, the comparison of the two controllers show that even though there is no visible difference in terms of levitation performance, LADRC is superior to PD/observer in disturbance rejection. It is the belief of the author that the HSS magnetic bearing control would benefit from the implementation of LADRC, for slight disturbances are often present in any given system. The implementation of LADRC would neither have the drawback of the PID in terms of phase lag, nor does it require the flywheel to be equipped with backup passive bearings, as in the case of PD/Observer control currently used in NASA's HSS module.

Once the flywheel rotor is levitated into its equilibrium position, it will be spun to eventually attain its final operating speed. This process is described by a different physical model than the lumped mass model considered so far. Because the spinning involves angular acceleration, the rotor will exhibit vibrations, during which the rotor will deviate from its equilibrium position. The control during both the accelerating and steady state operation of the rotor require consideration of rotor vibration dynamics from a control perspective, which is presented in the next chapter.

CHAPTER IV

INVESTIGATION OF ROTOR VIBRATION DYNAMICS

4.1   Background

Closed loop control design relies on the investigations of open loop plant dynamics. The study of rotor vibration dynamics has occupied mathematicians and physicists since at least 1919 when Jeffcott [2] proposed a rotor vibration model that has since become the most studied model of its kind. It exhibits all the properties of synchronous vibration, the most common and deleterious vibration in rotor dynamics. Traditional approaches to rotor vibration analysis have focused on understanding the physical phenomenon of vibration. For the purposes of vibration control however, mere knowledge of physical phenomenon is not sufficient. Despite burgeoning interest within the controls engineering community in rotor vibration control, there is currently a lack of literature dedicated to the controls aspects of rotor vibration. A more systematic controls approach is needed to bridge the disciplinary gap of the physicist and the controls engineer.

The purpose of this chapter is to analyze the Jeffcott rotor vibration model from a control engineering perspective. The methods employed here rely on the input-output relationship, which corresponds closely to the design philosophy of practicing engineers.

4.2   Rotor Vibration Dynamics

Rotor vibrations are caused by mass imbalance, which is unavoidable due to imperfections caused during manufacturing. Imbalance occurs if the center of mass of the rotor is not coincident with its geometrical center (Figure 12).
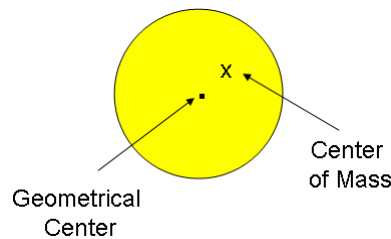
Figure 12: Top view of the rotor showing location of mass imbalance

In investigating rotor vibration dynamics, the most common model is the Jeffcott rotor [1]. The Jeffcott rotor is made up of a flat disk support by a uniform shaft, which is assumed to be massless. During operation, the rotor disk spins around its principal axis of inertia. Figure 13 shows the rotation geometry, where the principal axis of inertia is the z-axis (dashed lines). The rotor disk lies in the plane spanned by the x and y-axes. The angle of rotation is ϕ.
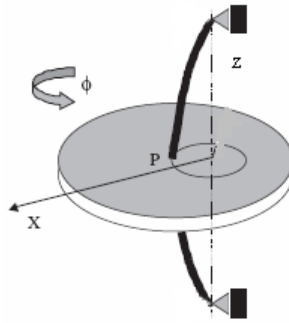
Figure 13: Rotation geometry of Jeffcott rotor

Because the center of mass is not located at the geometrical center of the rotor disk, a centrifugal force will be present on the rotor during rotation. The amplitude of this force is given by

$$F_c = me\dot{\phi}^2 \tag{4.1}$$

In equation (4.1), m is the total mass of the rotor, e is the distance from the geometrical center to the location of the imbalance (see Figure 14). Hence e is constant for a given rotor.

Figure 14: Rotation geometry (top view)

The set of differential equation of motion for the rotor can be derived from Newton's second law and centripetal force law [2]. In the absence of any external forces,

$$m\ddot{x} + kx + c\dot{x} = me\ddot{\phi}\sin\phi + me\dot{\phi}^2\cos\phi$$
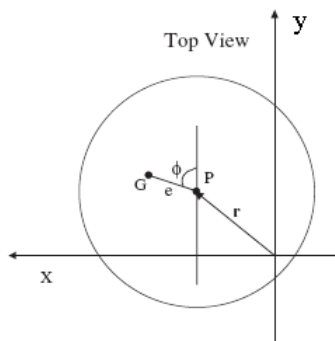$$m\ddot{y} + ky + c\dot{y} = -me\ddot{\phi}\cos\phi + me\dot{\phi}^2\sin\phi$$

(4.2)

The equations (4.2) describe the displacement of the geometrical center of the rotor in the *x* and *y* directions. In both equations, the three terms on the left hand side are the forces on the rotor shaft. The first term is the Newtonian force of acceleration. The second term is a restoring force similar to Hooke's law: if the rotor is displaced from the equilibrium position by amount *x*, then there is a force –*kx*, which tends to restore the rotor back to its equilibrium position. The third term is a damping force. Taken together, the three terms on the left hand side can be modeled as a second order mass-spring-damper system. In equation (4.2), the terms on the right hand side are the forces due to rotation. The first right hand term is the Euler force. It is present only if the angular acceleration is non-zero. The second right hand term is the centrifugal force which is proportional to the square of angular velocity. The equations (4.2) give the dynamics of the rotor in the absence of any external or control forces.

During the operation of the flywheel, the rotor will be spun from a zero initial rotation speed to a final speed. The rotation speed is usually measured in revolutions per minute (rpm). But $\dot{\phi}$ in (4.2) are given in radians per second (rad/s). Conversion from rpm to rad/s is often necessary.

$$1 rpm = 1\frac{revolution}{minute} = \frac{2\pi rad}{60\,s} = 0.1047(rad/s)$$

(4.3)

After the rotor reaches its final speed, it is in steady state. In that case, acceleration terms

vanish in equations (4.2), so that they reduce to:

$$m\ddot{x} + kx + c\dot{x} = me\dot{\phi}^2 \cos\phi$$
$$my\ddot{} + ky + c\dot{y} = me\dot{\phi}^2 \sin\phi$$
(4.4)

Since steady state operation is the final goal, most literature use equations (4.4). In the

present study, we will consider both steady state and accelerating operations. As a

general rule, evident from equation (4.1), higher speeds lead to greater centrifugal forces

due to imbalance.

4.3   Steady State Operation

Equations (4.4) can be solved to obtain rotor position in steady state, at which the angular

speed is constant, that is, $\dot{\phi} = w$.

$$m\ddot{x} + kx + c\dot{x} = mew^2 \cos wt$$
$$m\ddot{y} + ky + c\dot{y} = mew^2 \sin wt$$
(4.5)

The analysis of the time-variant differential equations (4.5) can be facilitated from a new

controls point of view by considering the centrifugal force as a disturbance input, and the

rotor position as the output,

$$m\ddot{x} + kx + c\dot{x} = F_{c,x}$$
$$m\ddot{y} + ky + c\dot{y} = F_{c,y}$$
(4.6)

and the disturbance transfer functions can be obtained through taking the Laplace

transform of equations (4.6):

41

$$\frac{X(s)}{F_{c,x}(s)} = \frac{1}{ms^2 + cs + k}$$

$$\frac{Y(s)}{F_{c,y}(s)} = \frac{1}{ms^2 + cs + k}$$

(4.7)

This shows that the disturbance transfer functions are identical for both coordinates x and y. Equations (4.7) is a linear time-invariant (LTI) second order system. The input disturbance forces $F_{c,x}(s), F_{c,x}(s)$ are sinusoids. A fundamental theorem concerning the response of LTI systems states that if the input into the system is a sinusoid, then the output of the system is a sinusoid of the same frequency In view of equations (4.7), this theorem implies that the rotor position behaves in terms of a sinusoid of the same frequency w of rotation. This can be seen in a time domain simulation of the system described by equations (4.5). Figure 15 and Figure 16 show the time domain steady state response of the rotor, in both x and y direction. The frequency of rotation is $w = 1$ rad/s. The system parameters are: $m = 1$ kg, $k = 4$ N/m, $c = 1$ Ns/m. The eccentricity $e = 0.001$m. From the figures the period of oscillation is approximately T = 6.2s, which corresponds to a frequency of

$$w = \frac{2\pi}{T} \approx 1 rad / s$$
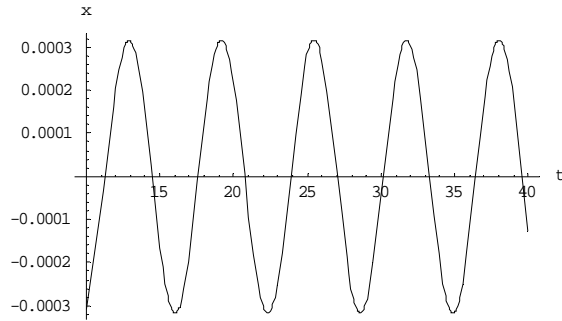
(4.8)

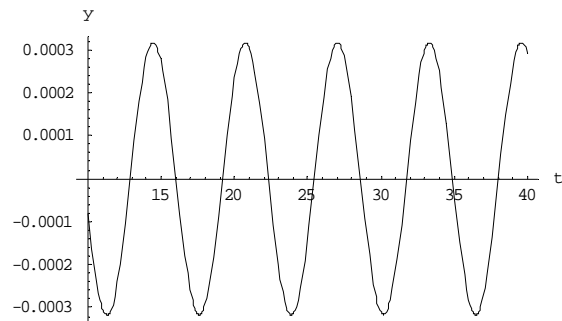**Figure 15: Time domain steady state response (x direction)**

Figure 16: Time domain steady state response (y direction)

Equations (4.5) can also be rendered in a parametric plot, which traces the orbit of the rotor center in the x-y plane. Figure 17 shows that the orbit of the rotor in steady state is a circle.
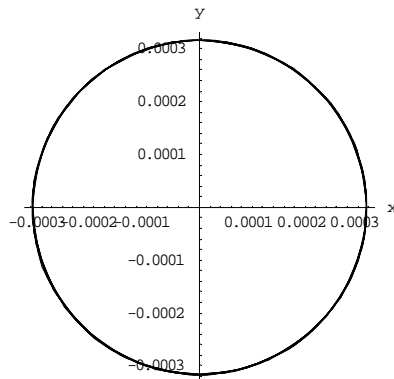

Figure 17: Rotor orbit (parametric plot) with w=1 rad/s

The controls perspective analysis of equations (4.7) also reveals that the second order system encounters resonance if the rotor spins at the frequency

$$w_n = \sqrt{\frac{k}{m}} \tag{4.9}$$

At the frequency w_n (referred to as the resonant or natural frequency), the rotor orbit will reach maximum amplitude. This property of system response has important implications on the controls aspects of rotor vibrations; in the following, both computational methods and control-analytical methods shall be employed to investigate the phenomena associated with resonance. Using the same system parameters for the simulation of Figure 15, Figure 16 and Figure 17, we arrive at the resonant frequency for our system:

$$w_n = \sqrt{\frac{4}{1}} = 2 rad/s \tag{4.10}$$

Figure 18 shows the rotor orbit at the resonant frequency. Comparing Figure 18 with Figure 17, the amplitude of oscillation at the resonant frequency is an order of magnitude higher than at w=1 rad/s.
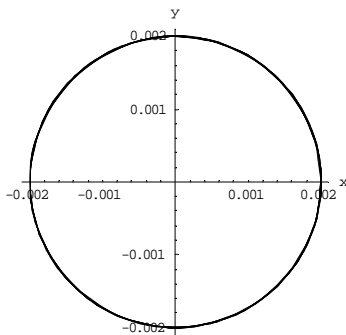
Figure 18: Rotor orbit with w=2 rad/s

Figure 19 shows the rotor orbit at a frequency higher than the resonant frequency. The rotor orbit amplitude has decreased with respect to the amplitude in Figure 18. This computational result demonstrates the fact that the rotor orbit reaches its maximum at the resonant frequency of the system.
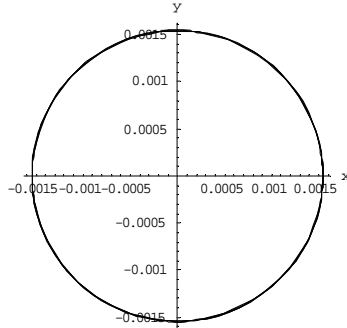
Figure 19: Rotor orbit with w=3 rad/s

The dependence of rotor orbit amplitude on the frequency of rotation can be analyzed using controls theoretical methods. Without loss of generality, only the equation of motion for the y coordinate is considered. The lower one of equation (4.7) can be rearranged as

$$Y(s) = \frac{1}{ms^2 + cs + k} F_{c,y}(s) \tag{4.11}$$

Where the disturbance force $F_{c,x}(s)$ is given by

$$F_{c,y}(s) = \int_0^\infty [mew^2 \sin wt] e^{-st} dt = mew^2 \frac{w}{s^2 + w^2} \tag{4.12}$$

$$Y(s) = \frac{1}{ms^2 + cs + k} \frac{mew^3}{s^2 + w^2} \qquad (4.13)$$

Equation (4.13) can now be plotted in frequency domain, using familiar frequency response methods in linear controls theory [23]. The system parameters are the same used to generate Figure 15 and Figure 16. The result is a Bode magnitude plot of Y(s), which is a measure of the amplitude of the rotor orbit. Figure 20 indicates that the largest amplitude occurs at w = 2 rad/s (noting that the frequency is plotted in log scale), where the magnitude of Y(s) exhibits a sharp peak. This is the resonance phenomenon observed in second order systems in controls theory.

The above analysis has recast steady state vibration dynamics in a familiar controls perspective. The next section will make extensive use of this analysis to examine different methods of rotor vibration control.
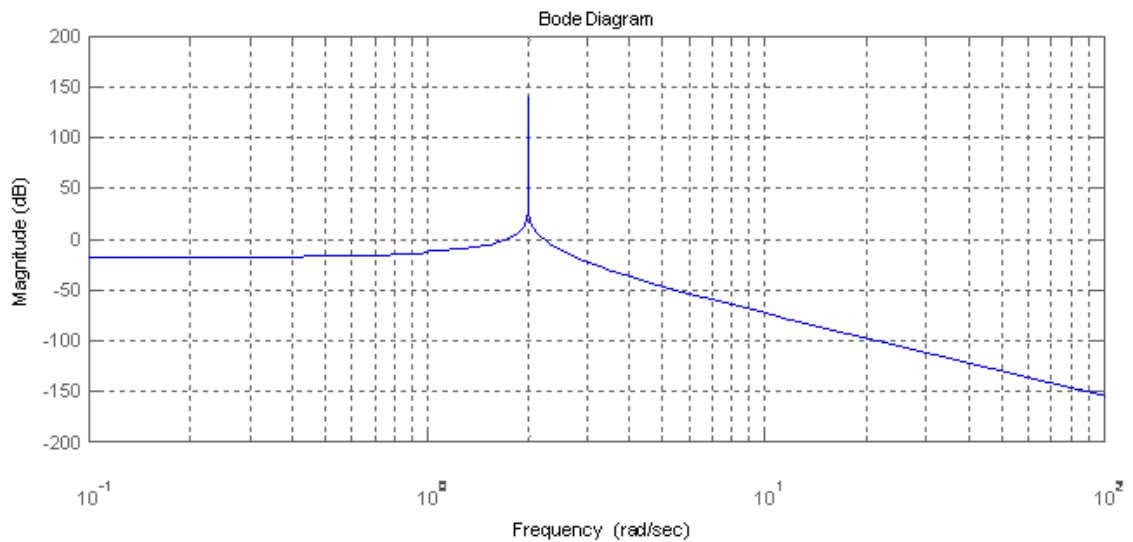

Figure 20: Bode magnitude plot

4.4   From Vibration Dynamics to Vibration Control

As mentioned in the preceding sections, the physical cause of vibrations is the centrifugal force exerted by a mass imbalance in the rotor. The effect of this centrifugal force on the rotor in steady state operation is expressed by equations (4.4). Because the rotor is spinning at constant speed, the centrifugal force term is a sinusoid of the same frequency as the rotation. This term causes the rotor to follow a circular orbit, which is a manifestation of synchronous vibration. Mathematically speaking, rotor vibration can thus be suppressed by canceling out the centrifugal force term. From a control perspective, this can be achieved by incorporating a physical actuator, which exerts an additional force $\bar{\mathbf{u}}$ on the system (4.4).

$$
\begin{aligned}
m\ddot{x} + kx + c\dot{x} &= mew^2 \cos wt - u_x \\
m\ddot{y} + ky + c\dot{y} &= mew^2 \sin wt - u_y
\end{aligned}
\tag{4.14}
$$

The force $\bar{\mathbf{u}}$ is referred to as the *actuation force*. The objective is to design a closed-loop control system such that the actuation force cancels out the centrifugal force term. In practice however, physical limitations on the actuator may prevent satisfactory achievement of this objective. It is thus necessary to examine the nature of the actuation force required to successfully cancel out the centrifugal force term; only so one can have an idea what physical device is needed for an actuator. The analysis of rotor vibration dynamics can now be used for the examination of actuation force. The most pertinent observations are summarized:

1. The rotor orbit follows a sinusoid in each dimension (Figure 15 and Figure 16).

2. The amplitude of the sinusoid reaches its peak amplitude at the resonant frequency (Figure 20). Thus the centrifugal force has its largest effect on the rotor orbit at the resonant speed.

3. The frequency of the rotor response increases with rotor speed. The *frequency* of the actuation force needed to cancel out the centrifugal force term is thus largest at the final operating speed (compare Figure 21 and Figure 22).
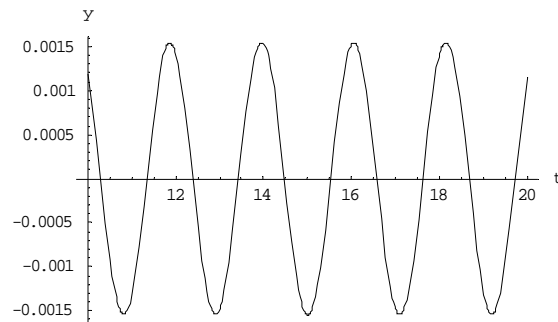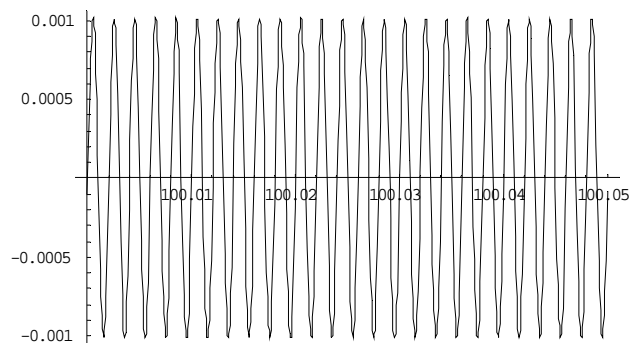

Figure 21: Time domain response (w = 3rad/s)

Figure 22: Steady state response at final operating speed (w = 30000 rpm)

4.5   Rotor Vibration Control

Since the rotor imbalance force is synchronous in nature, having the same frequency as the flywheel rotation, the actuator needed to reject the imbalance force necessary needs to work at the same frequency. Event though AMB is considered the fastest non-contact actuator currently available, its actuation speed is limited by the power bandwidth of the magnets.   Thus regardless of the control algorithm used, there will be issues with actuation frequency at high rotor speeds. Industrial flywheel rotors commonly operate at 30000 rpm. The aerospace flywheel currently in design by GRC is to reach an operating speed of 60000 rpm , which uses PD for vibration control. Their design philosophy is to use a controller that can be easily tuned. In keeping with this important practical goal, we apply Active Disturbance Rejection Control (ADRC) to address vibration issues and compare the results with PD control with a velocity observer. Both controllers will be parameterized by the same technique described in Chapter III, which renders them equally easy to tune. Thus, for a fair comparison, they can be simply compared in terms of performance and control effort. The goal is to assess whether ADRC outperforms PD in vibration control. The simulations are divided into two sections. First, the accelerating operation is addressed; second, the steady state operation is addressed.

Both operation cases are simulated according to equations (4.2). Since the two equations are independent, each one can be controlled separately, using the same control structure. For the purpose of comparisons, only the first one for the rotor motion in the x direction will be considered. The plant parameters are $m = 1$ kg, $k = 4$ N/m, $c = 1$ Ns/m, $e = 0.001$m. The simulation is carried out according to

$$m\ddot{x} + kx + c\dot{x} = me\ddot{\phi}\sin\phi + me\dot{\phi}^2\cos\phi \qquad (4.15)$$

The rotor orbit during accelerating operation is complex, despite the fact that it reaches a quasi-steady state, circular orbit after an amount of time. The behavior at the resonant speed can be seen through the outmost arc reaching an amplitude of 1.5 m.
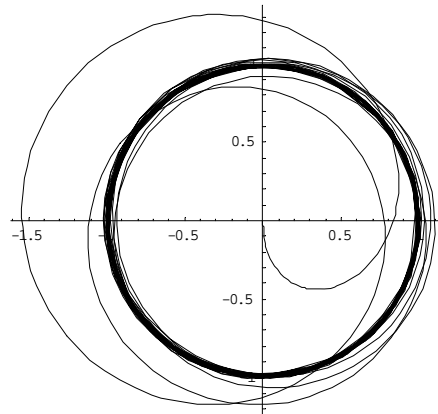
Figure 23: Rotor orbit during accelerating operation

The right hand side of the equation (4.15) is implemented as a sinusoidal disturbance force F_x which is injected into the plant (4.7). In the simulation, the rotor is spun from zero speed to its final speed, within t = 10s. During this time, the motion profile of ϕ is taken as a constant accelerating motion.

$$\begin{aligned} \ddot{\phi} &= a \\ \dot{\phi} &= at \\ \phi &= \frac{1}{2}at^2 \end{aligned} \qquad (4.16)$$

For t > 10s, the rotor achieves its steady state operation, and the speed is $\dot{\phi} = \omega = $ constant. In the first simulation, the final speed is chosen $\dot{\phi} = \omega = 100$ rad/s. The corresponding acceleration is $a = \omega / t = 10$ rad/s^2. The rotor displacement of open loop, with PD/Observer and LADRC are depicted in Figure 24. The controller and observer bandwidths are $wo = 1000$, and $wc = 200$, respectively.

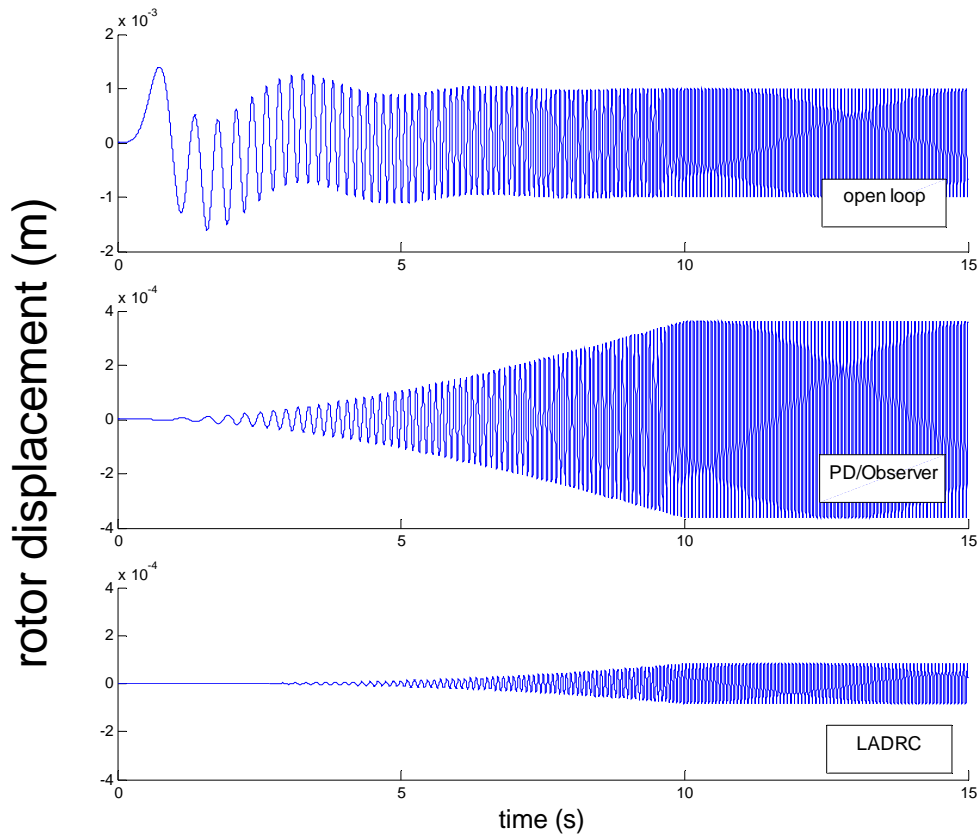**Figure 24: Rotor displacement comparison, $\omega = 100$ rad/s**

In the upper graph of the figure, the resonant peak can be clearly seen at t ≈ 1s, when the rotor passes through the critical speed at 2 rad/s (according to equation (4.9)). The amplitude of open loop vibration is greatest, and it clearly exceeds the air gap distance of 1mm. In an actual flywheel system, this would cause the rotor to touch the bearing and

thus cause catastrophic system failure. Due to the synchronous nature of vibration, the frequency of the vibration is 100 rad/s. Both controllers do very well to reduce the vibration during the resonance, as seen in the lower two graphs of Figure 24. They are both able to reduce the vibration amplitude by an order of magnitude. However by comparison among themselves, the rotor displacement amplitude with LADRC is four times less than that with PD/Observer.

An interesting property of both control performances is that at higher speeds, the vibration amplitudes tend to grow larger, even though this is not the case in the open loop system. As the rotor reaches its final operating speed, the amplitudes stop growing.

In terms of control effort, the two controllers are similar (see Figure 25), an even upon close inspection, the LADRC actuation force is only 2N lower than that of the PD/Observer (Figure 26). The zoomed in figure allows one to measure the actuation frequency of the controllers. Both controllers measure to be around 104 rad/s, which is in good agreement with the rotation frequency of 100 rad/s. This frequency can be easily achievable with currently available power amplification devices. For instance, the example of power electronic amplifier given at the end Chapter II would suffice for this application.
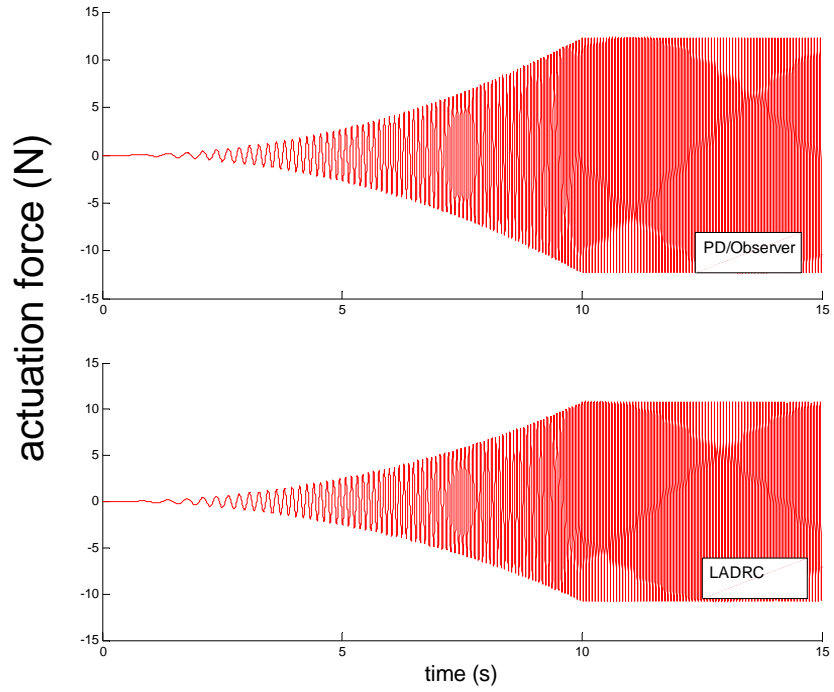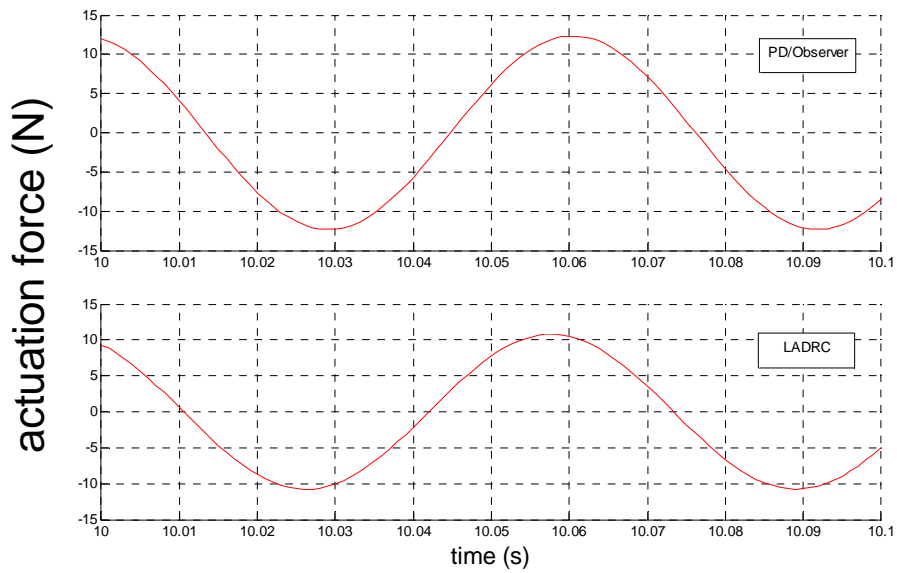
Figure 25: Actuation force comparison, ω = 100 rad/s

Figure 26: Actuation force comparison (zoomed in), ω = 100 rad/s

A note on the controller bandwidth should be given. Naturally, the performance of both controller can be improved by increasing the bandwidths *wo* and *wc*. But with increasing speed, the performances of both controllers will deteriorate. For instance, if the speed is increased to $\dot{\phi} = \omega = 1000$ rad/s, and the bandwidths kept at the same values as before, then there will be no difference in rotor amplitude at the steady state between open loop and closed loop control. Moreover, both controllers will have similar unacceptable performance corresponding to a vibration amplitude of 1mm. Thus in order to increase the controller performance at higher speeds, the bandwidths must be increased.

In the following simulation, the rotor speed is increased to a high speed of 60,000 rpm ($\omega = 3142$ rad/s), which is the maximum operating range of NASA's High Speed Shaft, currently under development. In order to handle the high frequency disturbance, the bandwidths are generously increased to *wo* = 1,000,000, and *wc* = 200,000. The angular acceleration is $a = \omega/t = 314.2$ rad/s^2. Due to the very high frequency at the steady state, the oscillations are no longer distinguishable on the graph. But Figure 27 still retains the same shape as Figure 24, even the amplitudes of the open loop vibrations are the same in steady state (still measuring 1mm). This confirms that the vibration dynamics is essential the same at both speeds. When zooming in on Figure 27, the vibration frequency can be estimated to be about 3142 rad/s.

The performances of the controllers are given in the lower two graphs of Figure 27. As in the lower speed case, both controllers handle the transient vibrations well, but in the steady state, their oscillation amplitude increase. The PD/Observer reduces the open loop

vibration by two orders of magnitude, whereas the LADRC reduces it by three orders of magnitude.
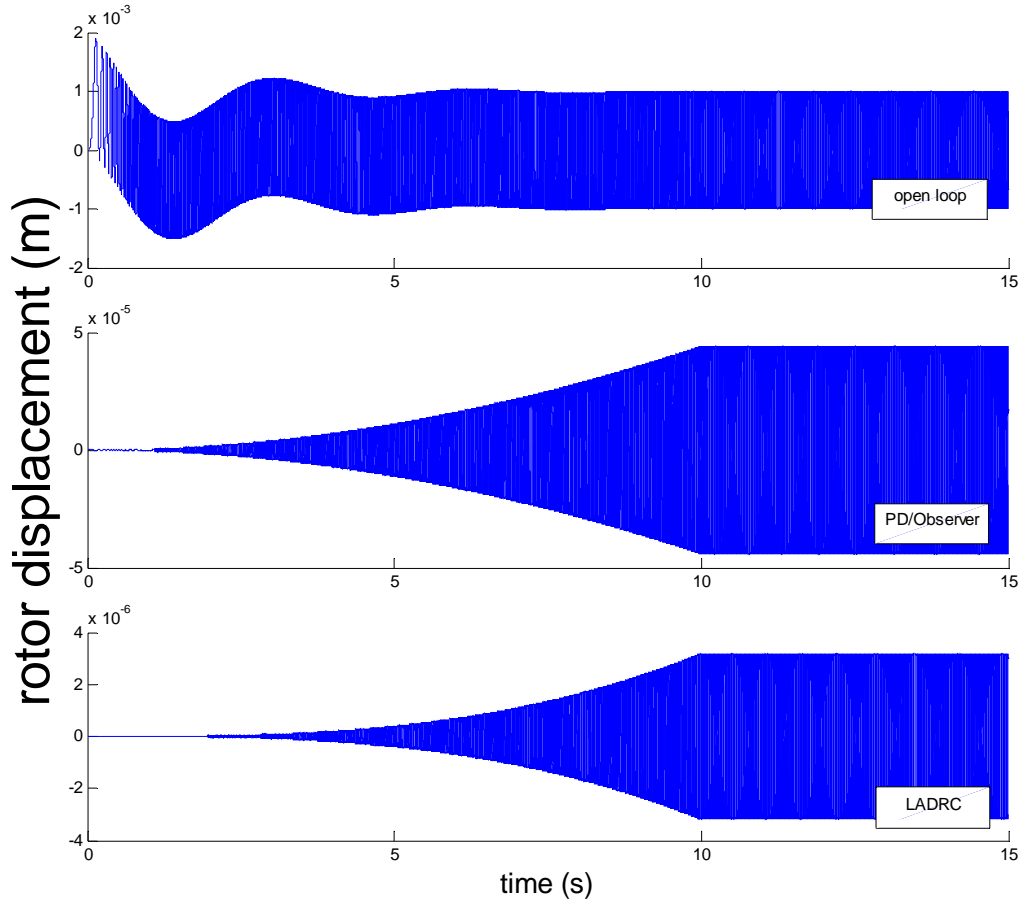
Figure 27: Rotor displacement comparison, $\omega = 3142$ rad/s (60,000 RPM)

The two controllers give rise to very similar actuation forces (Figure 28). The amplitude of this force is on the order of 10^4 N in steady state. The frequency is 3142 rad/s. State of the art power amplifiers are capable of achieving such magnitudes and frequency.

Figure 28: Actuation force comparison, ω = 3142 rad/s

Figure 29: Actuation force comparison (zoomed in)

Together, these simulation results give convincing evidence that ADRC outperforms PD/Observer in this lumped mass model of rotor vibration. In the following chapter, ADRC is applied to a three-degree-freedom distributed three-mass model of the rotor bearing system.

CHAPTER V

THE DISTRIBUTED MASS MODEL FOR ROTOR VIBRATION CONTROL

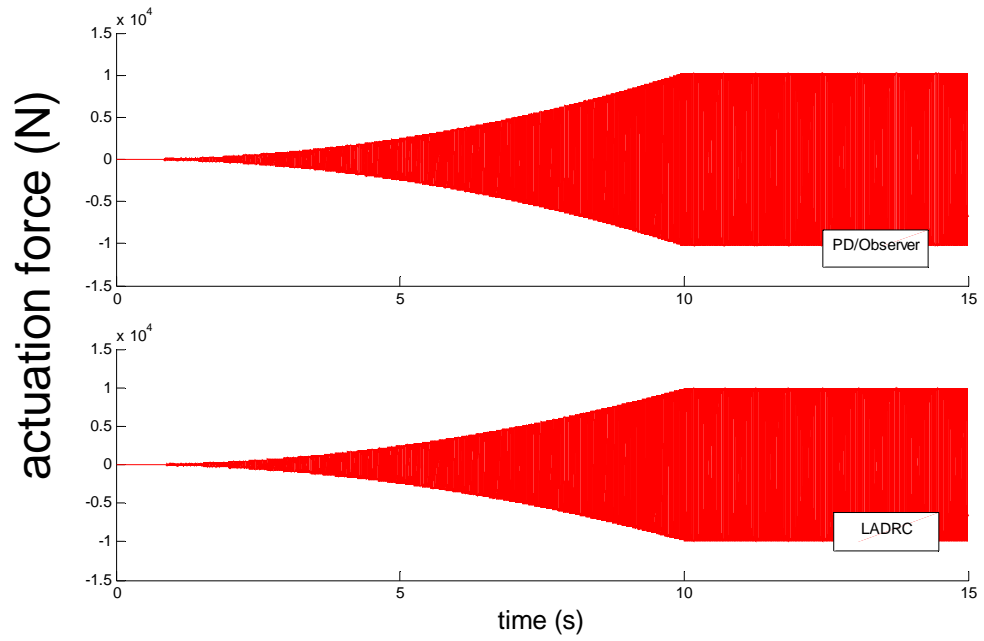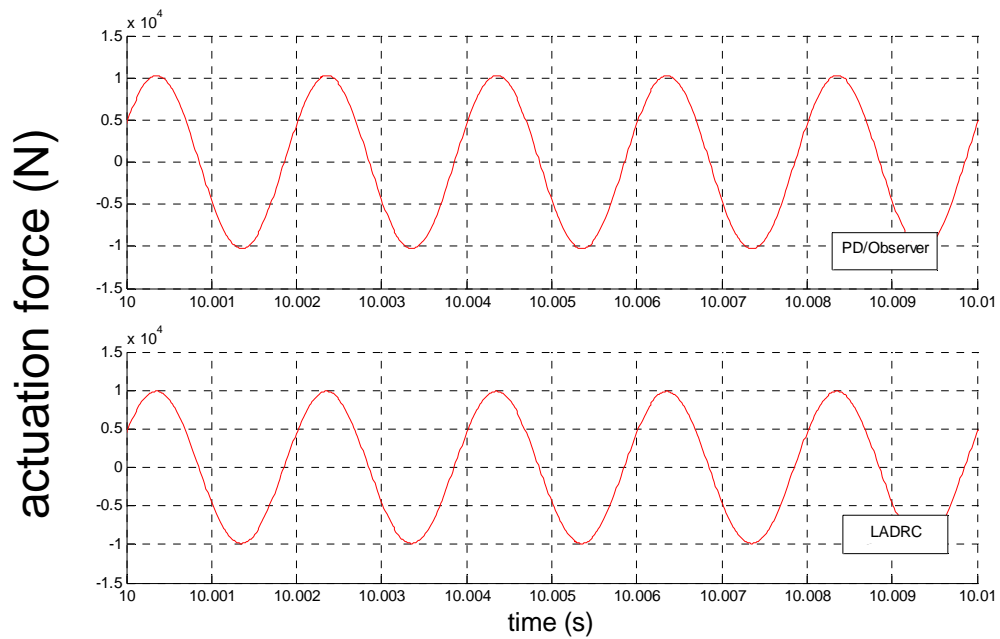Flywheel control is an interdisciplinary field spanning both electrical and mechanical engineering. In particular, the flywheel rotor modeling is a very well known problem in vibration dynamics. Even though a one-degree-of freedom model of the flywheel rotor can be used for control purposes, a multiple-degree-of freedom model comprised of a distributed mass system gives rise to greater accuracy. Also, for the actual implementation of the controller, such a model is more ideal, since more than one pair of magnetic bearings are used in practice. This makes the control problem essentially multiple input multiple output (MIMO).

In the following, a distributed three-mass model of synchronous vibration of the rotor-shaft system is presented. The system has three inputs and three outputs, and couplings between the three modes exist. The control solution for this problem comprises three

single-output ADRC loops running in parallel. The single-degree-of-freedom ADRC can be straightforwardly extended to cope with this MIMO problem. The noise sensitivity of ESO is also explored in this study.

5.1 Model and Open Loop Simulation

Synchronous rotor vibration can be modeled as a flexible shaft (simply supported) which is exposed to a sinusoidal rotor imbalance force. The simply supported beam is chosen because the magnetic bearings used in flywheel control provide flexible support. In this study, the distributed three-mass model is used (Figure 30). This model includes both the rotor (m2) and the shaft (m1, m3). According to the vibration analysis of a distributed system[1], even this simple three-mass model can provide a fair approximation for the first three modes of vibration.
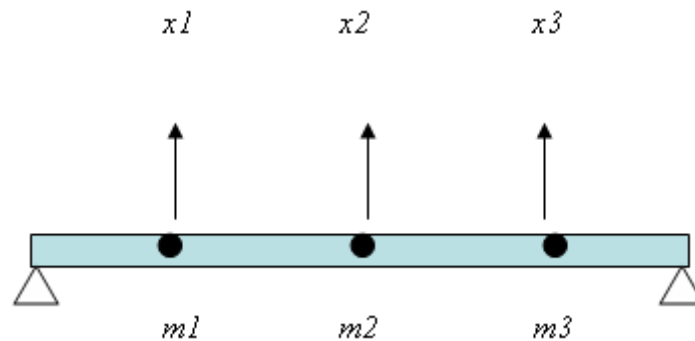

Figure 30: Simply supported beam modeled by three lumped masses

The general equation of motion for such a distributed system is

$$\mathbf{M}\ddot{\mathbf{x}} + \mathbf{C}\dot{\mathbf{x}} + \mathbf{K}\mathbf{x} = \mathbf{F}(t) + \mathbf{u} + \mathbf{Q}(t) \tag{5.1}$$

---

[1] *Vibration of Mechanical and Structural Systems*, James/Smith, 1 ed., p.388.

59

Where **M** is the mass matrix, **C** is the damping matrix and **K** is the stiffness matrix. For the system with three lumped masses, **x** is a vector of three degrees of freedom (x1, x2, x3), which gives the vertical displacement of the three masses as shown in Figure 30. The terms on the right hand side of equation (5.1) are the imbalance force **F**(t), and the control input **u**. Moreover, an external force **Q**(t) may be included, which can be used to model the imbalance torque caused by the motor. The mass and damping matrix contain only diagonal elements. The cross-damping terms are negligible. For the three-mass model, Equation (5.1) is a system of three equations, the first of which can be written out as

$$m_1\ddot{x}_1 + c_1\dot{x}_1 + k_{11}x_1 + k_{12}x_2 + k_{13}x_3 = f_1(t) + u_1 + Q_1(t) \tag{5.2}$$

and dividing by the mass on both sides of the equation yields the standard form:

$$\ddot{x}_1 + \frac{c_1}{m_1}\dot{x}_1 + \frac{k_{11}}{m_1}x_1 + \frac{k_{12}}{m_1}x_2 + \frac{k_{13}}{m_1}x_3 = \frac{f_1}{m_1} + \frac{u_1}{m_1} + \frac{Q_1}{m_1} \tag{5.3}$$

In order to simulate the plant using Matlab Simulink, equation (5.1) must be rendered in state space notation (equation (5.6)). That is, a state vector is defined as

$$X = [x_1, x_2, x_3, \dot{x}_1, \dot{x}_2, \dot{x}_3]^T \tag{5.4}$$

And equation (5.1) is recast in terms of the state vector, so that the resulting differential equation is first order. Equation (5.5) shows the state space representation of the system without control input and motor disturbance, whereas equation (5.6) contains all the inputs.

$$\frac{d}{dt}\begin{bmatrix} x_1 \\ x_2 \\ x_3 \\ \dot{x}_1 \\ \dot{x}_2 \\ \dot{x}_3 \end{bmatrix} = \begin{bmatrix} 0 & 0 & 0 & 1 & 0 & 0 \\ 0 & 0 & 0 & 0 & 1 & 0 \\ 0 & 0 & 0 & 0 & 0 & 1 \\ -\dfrac{k_{11}}{m_1} & -\dfrac{k_{12}}{m_1} & -\dfrac{k_{13}}{m_1} & -\dfrac{c_1}{m_1} & 0 & 0 \\ -\dfrac{k_{21}}{m_2} & -\dfrac{k_{22}}{m_2} & -\dfrac{k_{23}}{m_2} & 0 & -\dfrac{c_2}{m_2} & 0 \\ -\dfrac{k_{31}}{m_3} & -\dfrac{k_{32}}{m_3} & -\dfrac{k_{33}}{m_3} & 0 & 0 & -\dfrac{c_3}{m_3} \end{bmatrix}\begin{bmatrix} x_1 \\ x_2 \\ x_3 \\ \dot{x}_1 \\ \dot{x}_2 \\ \dot{x}_3 \end{bmatrix} + \begin{bmatrix} 0 \\ 0 \\ 0 \\ \dfrac{f_1}{m_1} \\ \dfrac{f_2}{m_2} \\ \dfrac{f_2}{m_3} \end{bmatrix} \qquad (5.5)$$

$$\frac{d}{dt}\begin{bmatrix} x_1 \\ x_2 \\ x_3 \\ \dot{x}_1 \\ \dot{x}_2 \\ \dot{x}_3 \end{bmatrix} = \begin{bmatrix} 0 & 0 & 0 & 1 & 0 & 0 \\ 0 & 0 & 0 & 0 & 1 & 0 \\ 0 & 0 & 0 & 0 & 0 & 1 \\ -\dfrac{k_{11}}{m_1} & -\dfrac{k_{12}}{m_1} & -\dfrac{k_{13}}{m_1} & -\dfrac{c_1}{m_1} & 0 & 0 \\ -\dfrac{k_{21}}{m_2} & -\dfrac{k_{22}}{m_2} & -\dfrac{k_{23}}{m_2} & 0 & -\dfrac{c_2}{m_2} & 0 \\ -\dfrac{k_{31}}{m_3} & -\dfrac{k_{32}}{m_3} & -\dfrac{k_{33}}{m_3} & 0 & 0 & -\dfrac{c_3}{m_3} \end{bmatrix}\begin{bmatrix} x_1 \\ x_2 \\ x_3 \\ \dot{x}_1 \\ \dot{x}_2 \\ \dot{x}_3 \end{bmatrix} + \begin{bmatrix} 0 & 0 & 0 & 0 & 0 & 0 \\ 0 & 0 & 0 & 0 & 0 & 0 \\ 0 & 0 & 0 & 0 & 0 & 0 \\ 0 & 0 & 0 & \dfrac{1}{m_1} & 0 & 0 \\ 0 & 0 & 0 & 0 & \dfrac{1}{m_2} & 0 \\ 0 & 0 & 0 & 0 & 0 & \dfrac{1}{m_3} \end{bmatrix}\begin{bmatrix} 0 \\ 0 \\ 0 \\ f_1 + u_1 + Q_1 \\ f_2 + u_2 \\ f_3 + u_3 \end{bmatrix} \qquad (5.6)$$

The rotor imbalance forces are sinusoidal:

$$\begin{aligned} f_1 &= m_1 e_1 w^2 \sin(wt), \\ f_2 &= m_2 e_2 w^2 \sin(wt), \\ f_3 &= m_3 e_3 w^2 \sin(wt) \end{aligned} \qquad (5.7)$$

The term Q_1 may be used to represent the imbalance torque caused by the motor. Since the motor is connected only to one side of the shaft, only the first mass point m_1

experiences this motor imbalance. In the most general case, we may assume the profile of this imbalance to be sinusoidal:

$$Q_1 = A\sin(w_1 t + \phi_1), \tag{5.8}$$

Where the motor disturbance frequency w_1 is different than the rotation frequency w. The amplitude and the phase depend on the nature of the disturbance.

Figure 31 is the Matlab Simulink setup. The State-Space block represents the system given by equation (5.5) and (5.7). We note that this setup is an *open-loop* simulation, because no control input has been added. (Also, this figure does not explicitly show the motor disturbance, however, the motor disturbance is included in the simulation.)
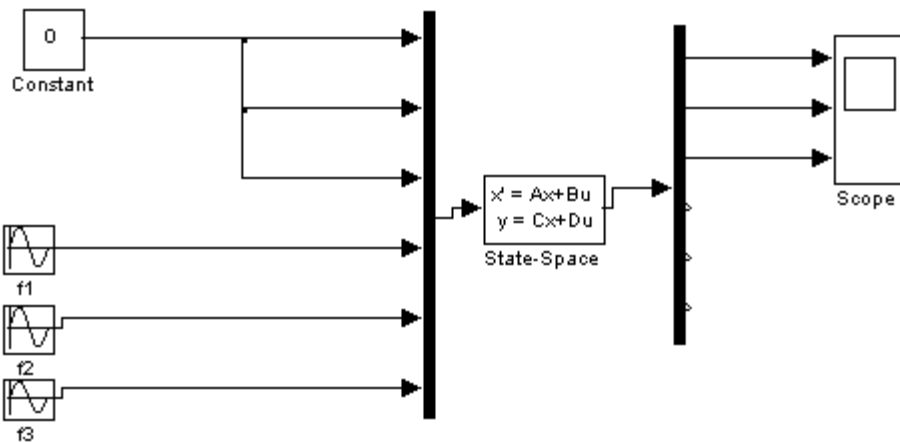

Figure 31: Matlab Simulink representation of the system given by equation (5.5)

The six inputs (to the left of the State-Space block) represent the third right hand side term in equation (5.5), namely, the imbalance forces. The six outputs (to the right of the

State-Space block) are the states of the vector (5.4). Only the first three terms (x1, x2, x3) are tracked.

For the open loop simulation, the angular frequency (which is the rotor speed) is w = 300 rad/s. The plant parameters are taken from an example in vibration literature.[2] The eccentricities are e1=e3=0.0001m, and e2=0.002m. The motor imbalance is

$$Q_1 = \sin(315t + \pi/10), \tag{5.9}$$

Thus, the motor imbalance is at a frequency slightly higher than the rotor speed, which leads to a phase shift with respect to the rotor imbalance forces (5.7).
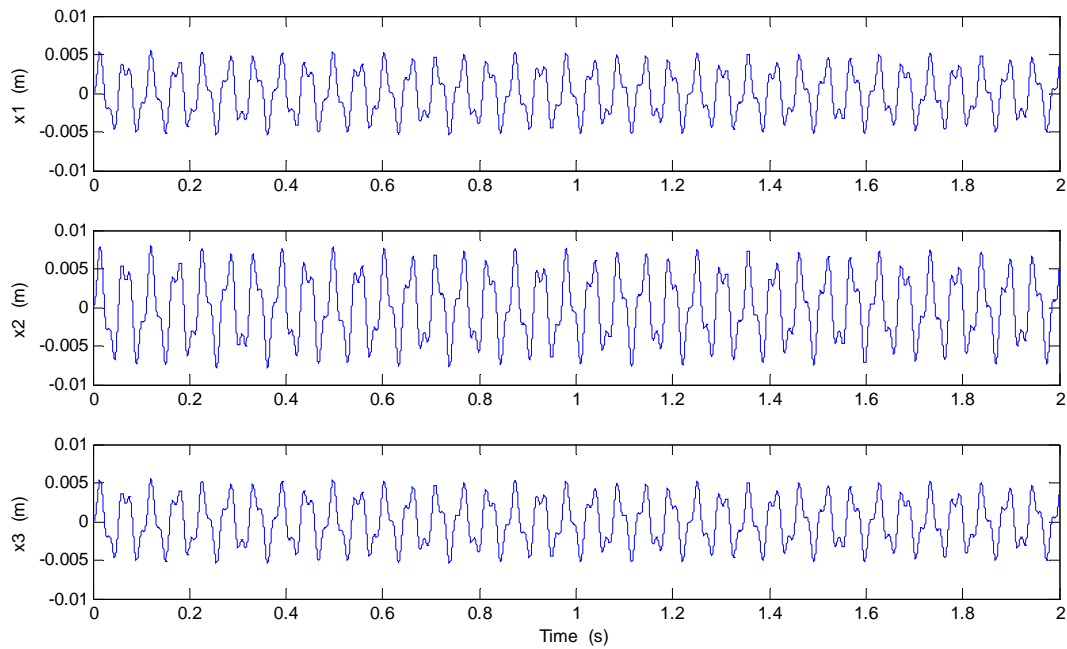

Figure 32: Open loop (displacement)

---

[2] *Vibration of Mechanical and Structural Systems*, James/Smith, 1 ed., p.387.

According to the open loop simulation results, the displacement x2 is the largest among the three, which represents the location of the rotor. All vibration amplitudes are in millimeter range. The amplitude of x1 and x3 reach 5×10^{-3}m, and that of x2 reaches 8×10^{-3}m.

5.2   Closed Loop Simulation Comparison

In the following, closed loop control of the system is analyzed. The simulation setup for typical closed loop control is shown in Figure 33. In the following graphs, PID control is compared to ADRC control in terms of reduction in vibration amplitudes (x1, x2, x3), as well as the control effort (u1, u2, u3). Both two-pair bearing configurations and three-pair bearing configurations are considered.

The same tuning parameters are used in all simulations. The tuning parameters of the PID controllers are: kp = $(10000)^2$, kd = $2 \times (10000)$, ki = 1000. The tuning parameters of the ADRC controllers are: Controller gains: wc1=wc3=40000, wc2=10000; Observer gains: wo1=wo2=wo3=80000.

5.3   Two-pair Configuration

The number of control inputs depends on the number of pairs of magnetic bearings used. Figure 34 and Figure 35 show the control performance of PID and ADRC with two pairs of bearings, positioned at m1 and m3. In other words, the second control input is zero, i.e., u2=0.

The PID control reduces the vibration amplitudes x1 and x3 to 5×10^{-5}m, which is two orders of magnitude lower than the open loop vibration. The amplitude of x2 is 2×10^{-3}m, which is only a four-fold reduction. The ADRC control performs slightly better. The amplitude of x1 and x3 are reduced to 4×10^{-5}m. However, there is no improvement over the PID for x2. The control efforts of both controllers are the same.

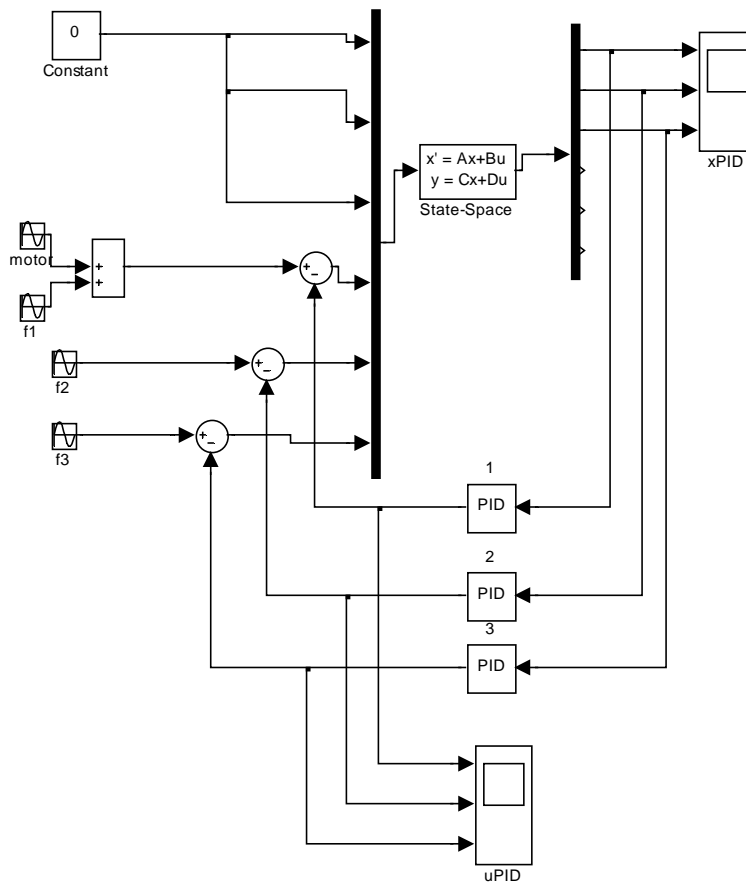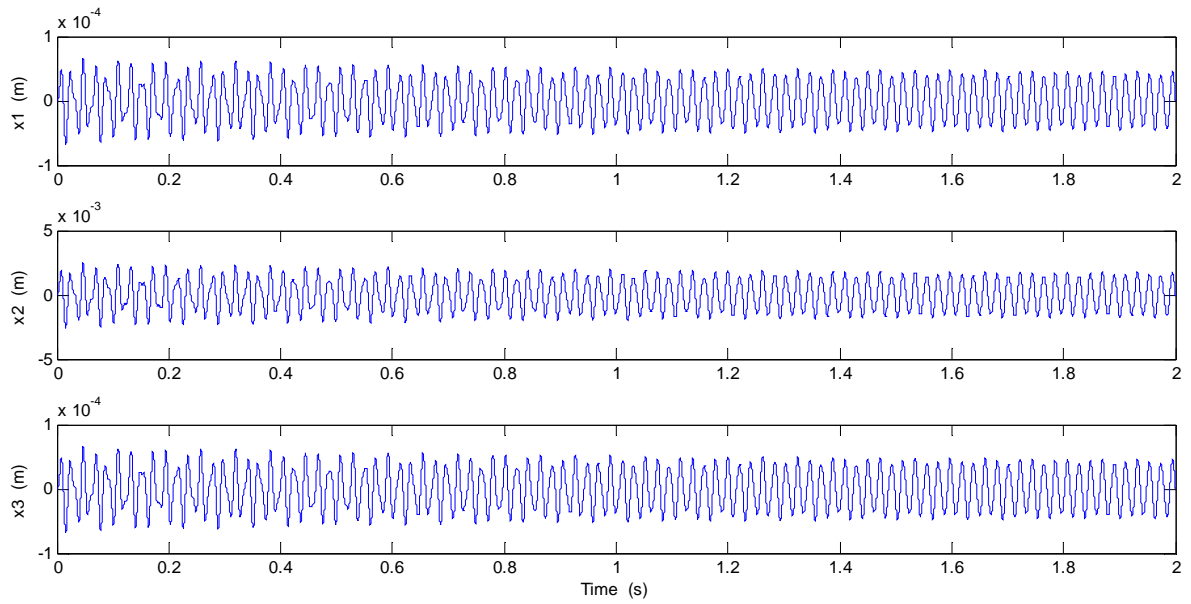**Figure 33: A Typical Closed Loop Control Simulation**

Figure 34: Two-Bearing PID Control (displacement)
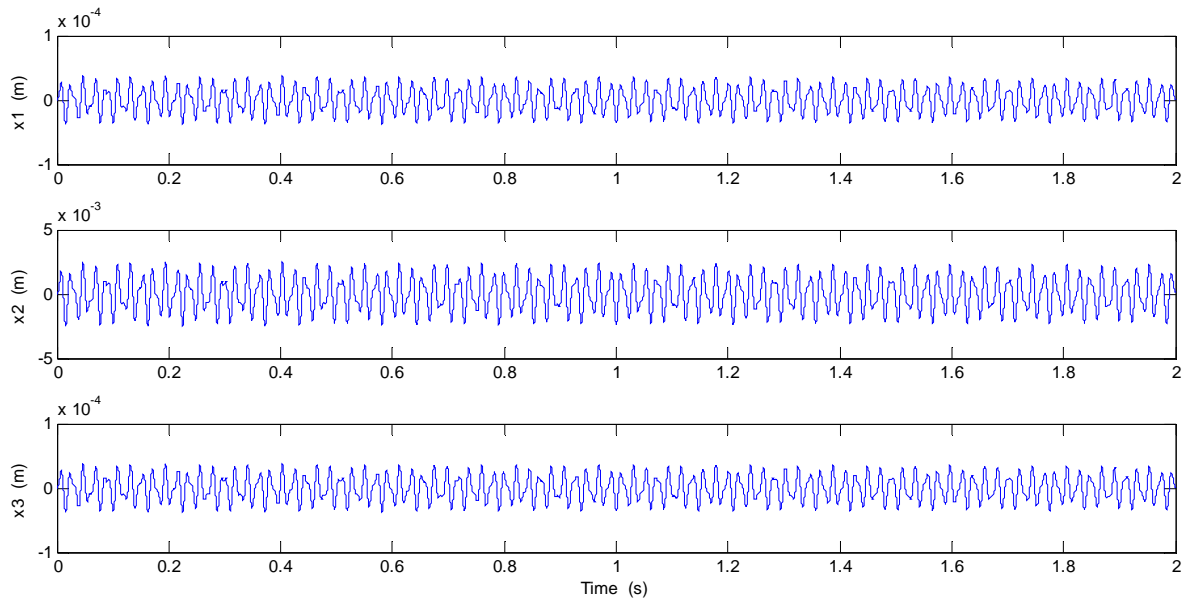
Figure 35: Two-Bearing ADRC Control (displacement)

66

5.4 Three-pair Configuration

If an additional third pair of magnetic bearings is positioned at m2, the control performance is drastically improved. Figure 36 and Figure 37 show the control performance of PID and ADRC with three pairs of bearings, positioned at m1, m2 and m3.
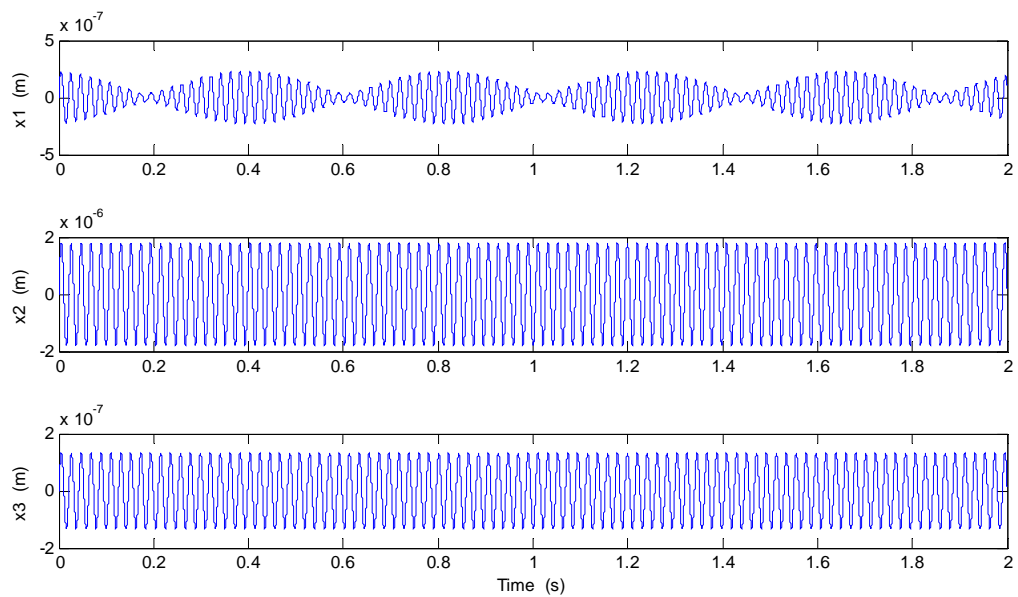
Figure 36: Three-Bearing PID Control (displacement)

As a general trend, three-bearing configuration achieves a four-order of magnitude reduction of vibration amplitude compared to open loop. In this configuration, the ADRC control is seen to significantly outperform the PID controller, given the same or lower control efforts (Figure 38).

Figure 37: Three-Bearing ADRC Control (displacement)

Figure 38: Three-Bearing PID Control (control effort)

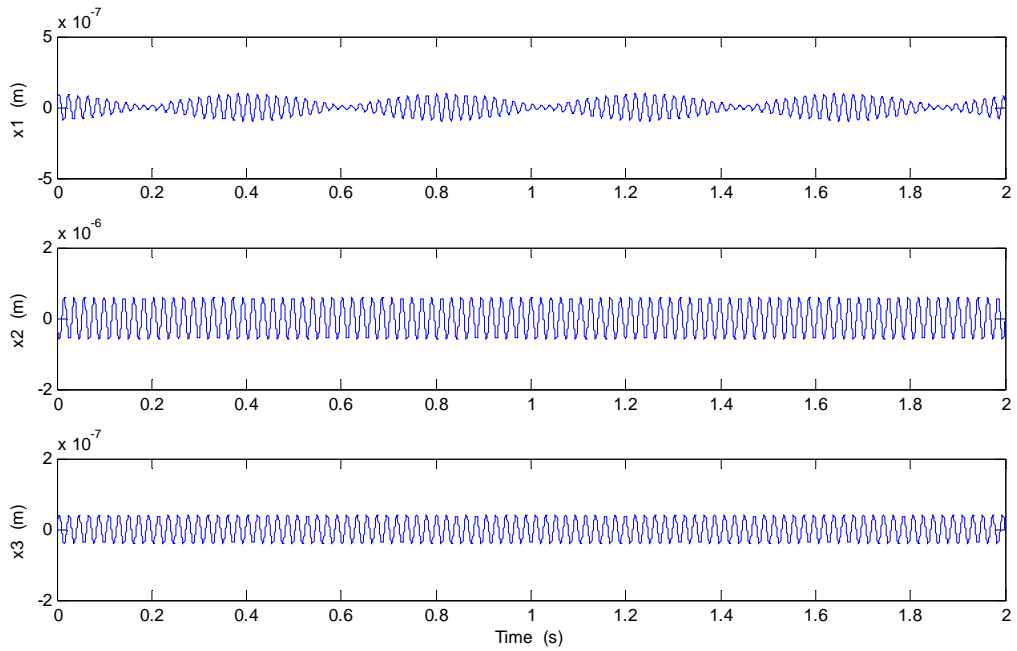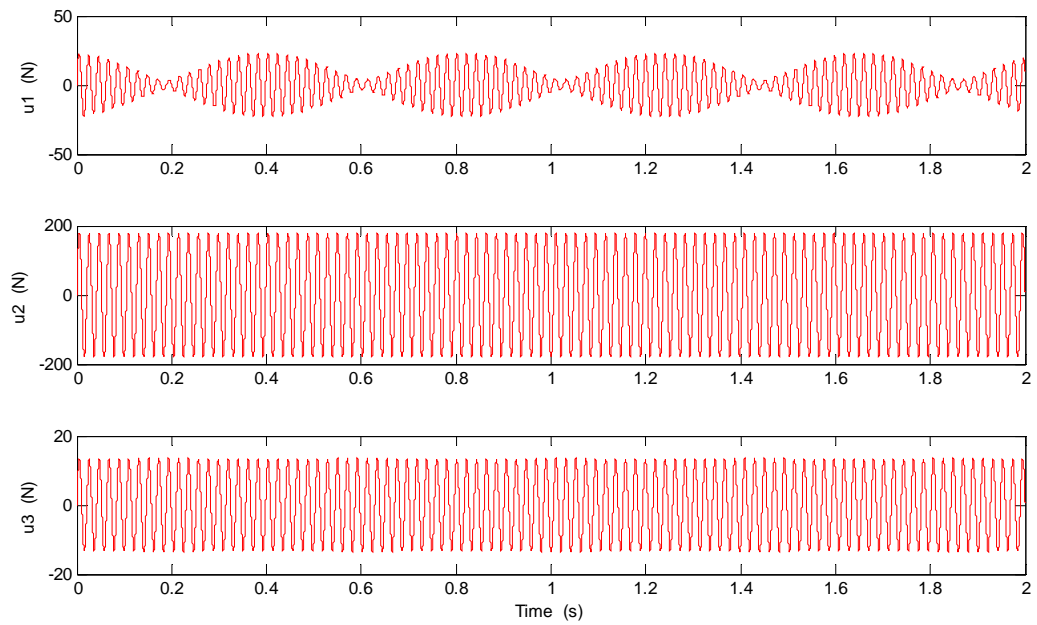*5.5   Rotor Vibration Control Simulation – Rotor Acceleration*

A start-up rotor undergoes angular acceleration before finally achieving its operating speed. For instance, the rotor may be required to reach an operating speed of 300 rad/s in 0.5 second, starting from zero initial speed. Such a case is termed accelerating or varying speed operation.   In flywheel energy storage applications, the rotor speed is to be regulated to achieve varying energy content, and therefore the varying speed operation must be addressed in the vibration control design.

The vibration dynamics of varying speed operation is more complex than the steady state case. As the speed varies, the rotor undergoes angular acceleration, and the imbalances forces are no longer simple sinusoids and do not solely depend on the angular velocity. Rather, they are of the form (5.10),

$$f = m \cdot e \cdot (\ddot{\phi} \sin\phi + \dot{\phi}^2 \cos\phi) \qquad (5.10)$$

where ϕ denotes the angle of rotation. If the angular speed is constant, i.e., $\dot{\phi} = w$, then equation (5.10) reduces to the imbalance force for steady state operation $f = mew^2 \cos wt$. To incorporate these imbalance forces into the three-lumped-mass model of the rotor (5.6), the imbalances forces are given in equation (5.7).

$$\frac{d}{dt}\begin{bmatrix} x_1 \\ x_2 \\ x_3 \\ \dot{x}_1 \\ \dot{x}_2 \\ \dot{x}_3 \end{bmatrix} = \begin{bmatrix} 0 & 0 & 0 & 1 & 0 & 0 \\ 0 & 0 & 0 & 0 & 1 & 0 \\ 0 & 0 & 0 & 0 & 0 & 1 \\ -\dfrac{k_{11}}{m_1} & -\dfrac{k_{12}}{m_1} & -\dfrac{k_{13}}{m_1} & -\dfrac{c_1}{m_1} & 0 & 0 \\ -\dfrac{k_{21}}{m_2} & -\dfrac{k_{22}}{m_2} & -\dfrac{k_{23}}{m_2} & 0 & -\dfrac{c_2}{m_2} & 0 \\ -\dfrac{k_{31}}{m_3} & -\dfrac{k_{32}}{m_3} & -\dfrac{k_{33}}{m_3} & 0 & 0 & -\dfrac{c_3}{m_3} \end{bmatrix}\begin{bmatrix} x_1 \\ x_2 \\ x_3 \\ \dot{x}_1 \\ \dot{x}_2 \\ \dot{x}_3 \end{bmatrix} + \begin{bmatrix} 0 & 0 & 0 & 0 & 0 & 0 \\ 0 & 0 & 0 & 0 & 0 & 0 \\ 0 & 0 & 0 & 0 & 0 & 0 \\ 0 & 0 & 0 & \dfrac{1}{m_1} & 0 & 0 \\ 0 & 0 & 0 & 0 & \dfrac{1}{m_2} & 0 \\ 0 & 0 & 0 & 0 & 0 & \dfrac{1}{m_3} \end{bmatrix}\begin{bmatrix} 0 \\ 0 \\ 0 \\ f_1 + u_1 + Q_1 \\ f_2 + u_2 \\ f_3 + u_3 \end{bmatrix} \quad (5.11)$$

$$f_1 = m_1 e_1 (\ddot{\phi}\sin\phi + \dot{\phi}^2 \cos\phi)$$
$$f_2 = m_2 e_2 (\ddot{\phi}\sin\phi + \dot{\phi}^2 \cos\phi), \quad\quad\quad (5.12)$$
$$f_3 = m_3 e_3 (\ddot{\phi}\sin\phi + \dot{\phi}^2 \cos\phi)$$

Where the angle of rotation ϕ is obtained by assuming constant acceleration.

$$\ddot{\phi} = a$$
$$\dot{\phi} = at \quad\quad\quad (5.13)$$
$$\phi = \frac{1}{2}at^2$$

In the simulation of the system, the angular velocity of the rotor will be varied from zero (rotor at rest) to 300 rad/s (operating speed) in 0.5 seconds. The angular velocity profile is shown in Figure 39.
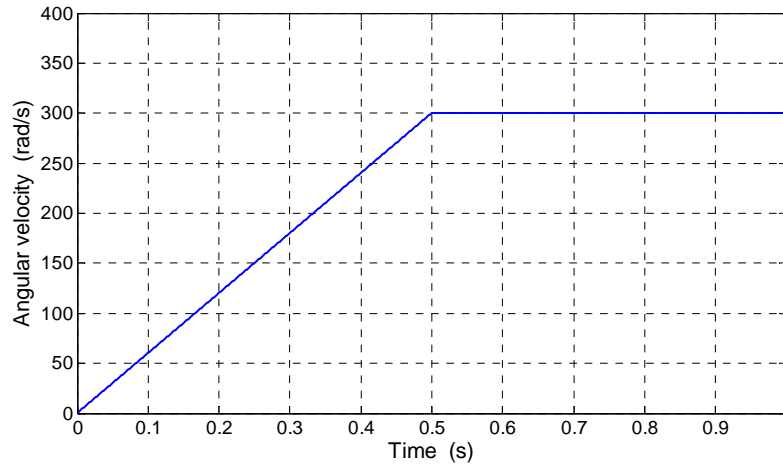
Figure 39: Angular velocity profile

The term Q_1 may be used to represent the imbalance torque caused by the motor. Since the motor is connected only to one side of the shaft, only the first mass point m_1 experiences this motor imbalance. In the most general case, one may assume the profile of this imbalance to be sinusoidal:

$$Q_1 = \sin(315t + \pi/10) \tag{5.14}$$

Note that the motor disturbance frequency w_1 is different than the operating frequency w. The amplitude and the phase depend on the nature of the disturbance.

5.6   Open loop simulation

The open loop vibration simulation (Figure 40) of the varying speed operation shows the general trend that the vibration amplitude grows with rotor speed, in accordance with (5.10). As with the steady state operation, the displacement of mass m2 is largest.

71

Figure 40: Open loop (displacement)

5.7   *Closed loop simulation*

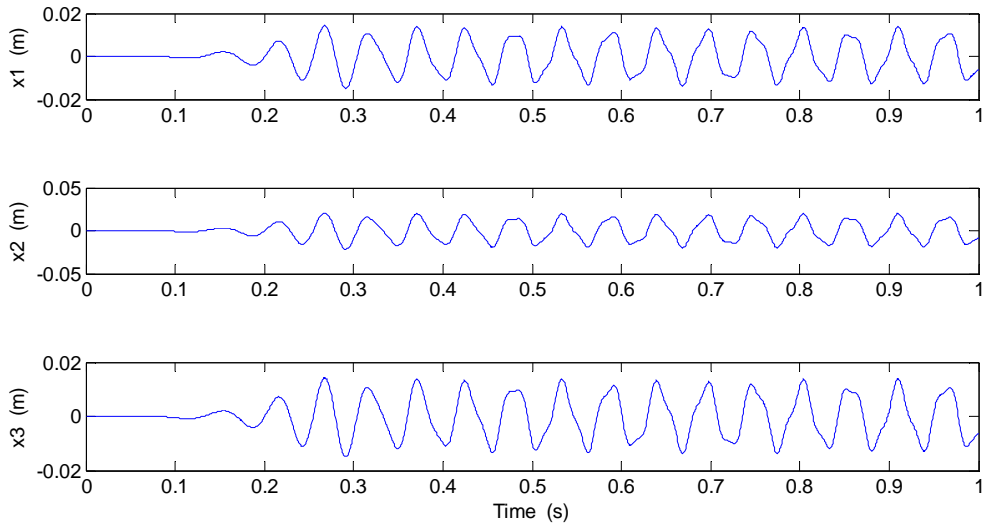When control is added, the vibration amplitude is decreased by several orders of magnitude, resulting in negligible vibrations. However, even with closed loop control, the vibration amplitude grows with the speed of the rotor. After the rotor reaches steady state operation (at t=0.5s), the displacement of the masses m2 and m3 exhibit simple sinusoidal motion. The displacement of mass m1 is still slightly affected by the motor torque disturbance. The control input is greatest at m2, due to the large mass located there (Figure 42 and Figure 44). Even though the magnetic bearings are required to deliver forces in the range from -300 to 300N, modern power amplifiers are capable of reaching both the required magnitude and frequency for the closed loop control system. The simulation comparisons also confirm ADRC's superior performance to PID in terms of vibration reduction, as well as control effort minimization. The following figures show

72

that the vibration amplitude associated with ADRC control is three to four times less than those of the PID control. A similar trend holds for the control input, save for u2, which is the same for both controllers.
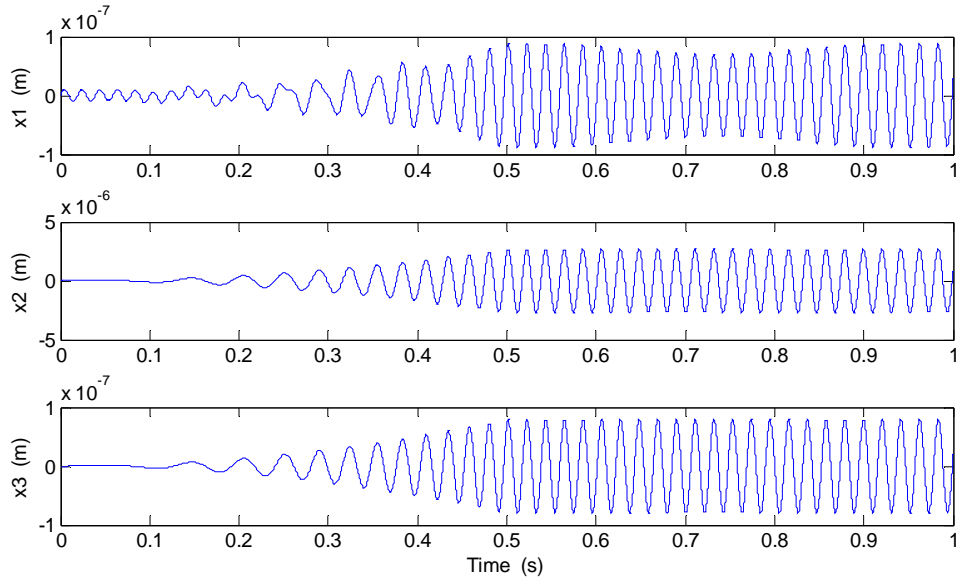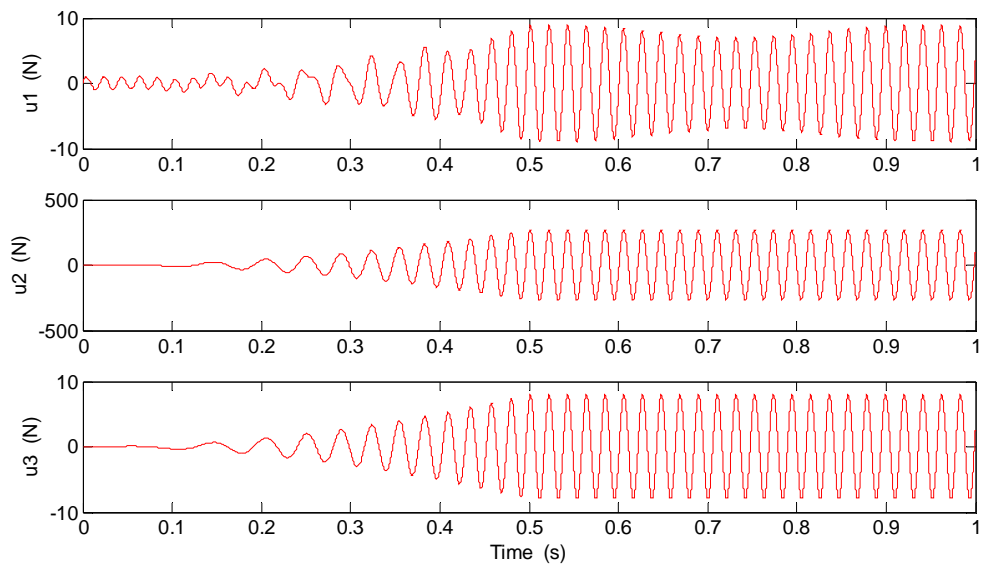

Figure 41: PID Control (displacement)
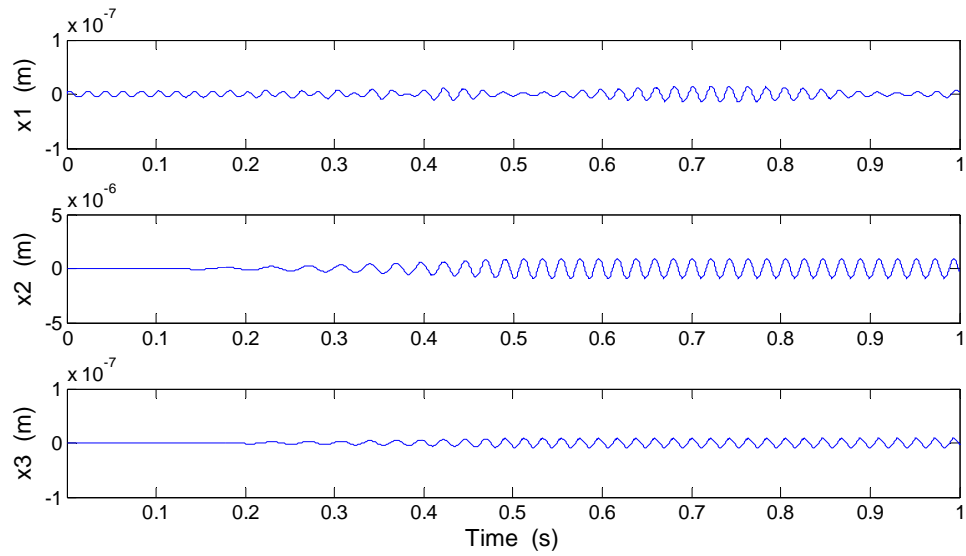

Figure 42: PID Control (control effort)

Figure 43: ADRC Control (displacement)
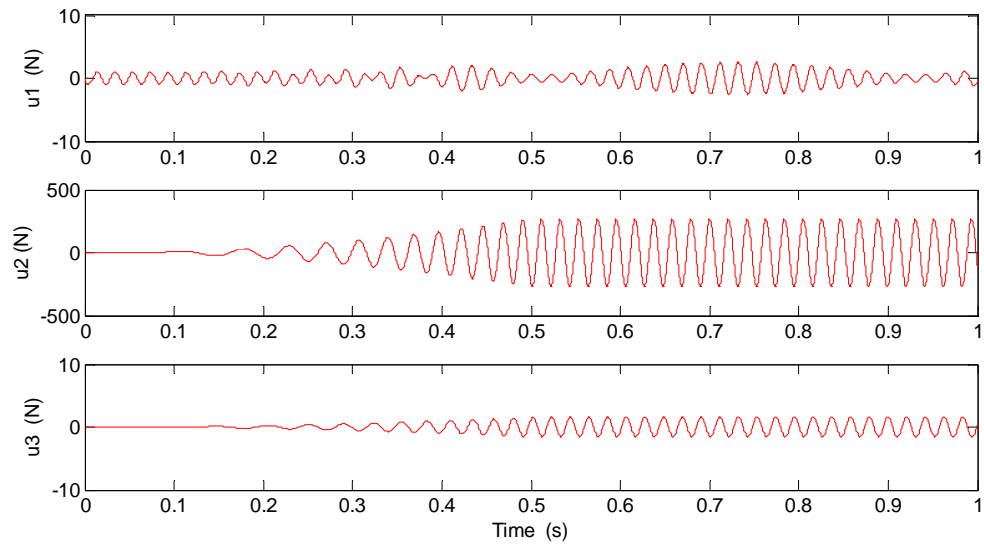
Figure 44: ADRC Control (control effort)

74

5.8   *ESO Noise Sensitivity*

The sensor used for detecting rotor vibration amplitude is not perfect, and in practice, the sensor signals are corrupted by noise. The presence of sensor noise can have a drastic effect on the closed-loop control performance. This effect is more drastic in the case of rotor vibration control, since the noise-free sensor signals of vibration amplitude are very small to begin with. It is thus necessary to make sure that our controller still operates well under the presence of significant noise. In the following, we will compare the effect of the observer and controller bandwidths on the noise in the closed loop performance. The addition of noise is achieved in Matlab simulink by the injection of band limited white noise, a random Gaussian noise generator with a Noise Power of 10^{-15}.

Figure 45 and Figure 46 demonstrate the noisy nature of the rotor deviation and AMB actuation force: both graphs exhibit random spikes, which are a manifestation of the sensor being corrupted with noise. An illustrative comparison between f and z3 in Figure 47 shows relatively accurate ESO tracking of the generalized disturbance. Even though both f and z3 are corrupted by noise, the spikes of z3 shows that ESO is more affected by noise.

75
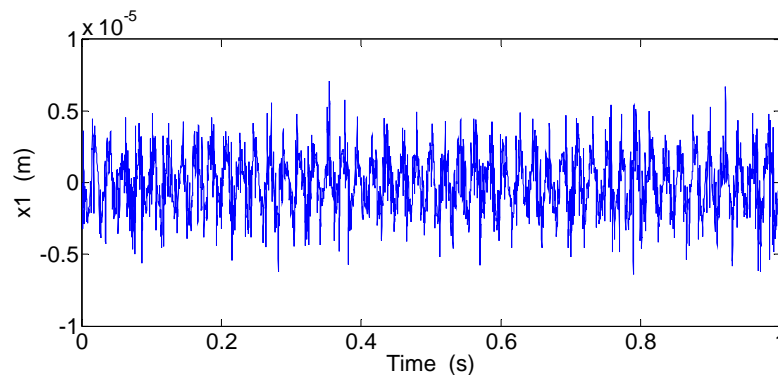
Figure 45: Closed-loop rotor vibration with sensor noise (wo=5000, wc=1000)
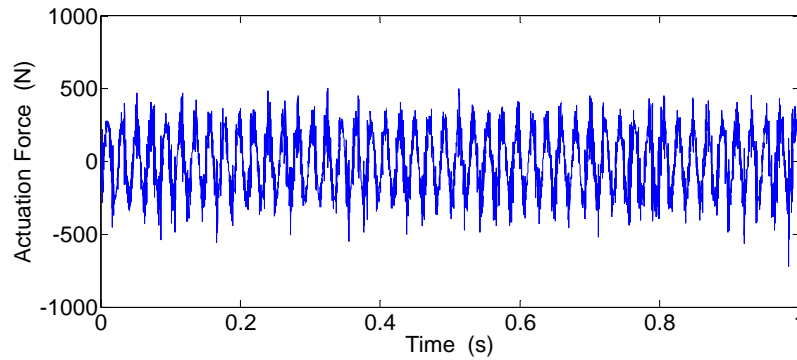
Figure 46: Actuation forces with sensor noise (wo=5000, wc=1000)
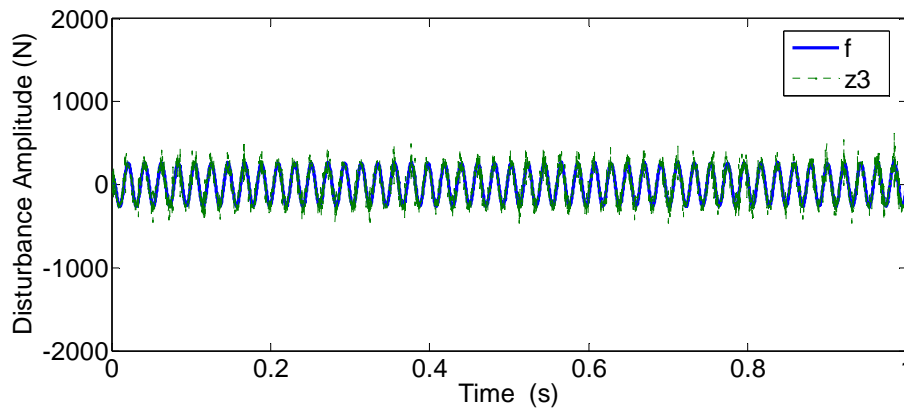
Figure 47: ESO tracking under noise (wo=5000, wc=1000)

Under noise free conditions, increasing the controller and observer bandwidths will normally lead to improved closed loop performance. However, in the presence of noise, increases in bandwidths could degrade the performance. This is most vividly shown in Figure 48. Here, both bandwidths are increased by an order of magnitude to wo=50000

and wc=10000. The resulting actuation forces in Figure 48 are much noisier and larger than the corresponding actuation forces at lower bandwidths (Figure 46). Also, the bandwidths increase directly affects the value of f and the performance of the ESO. In Figure 49, the noisy nature of both f and z3 have increased compared to Figure 47.
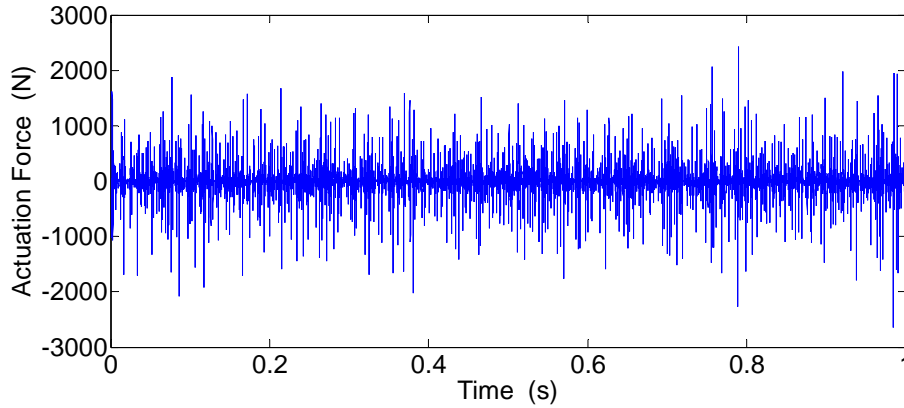
Figure 48: Actuation forces with sensor noise (wo=50000, wc=10000)
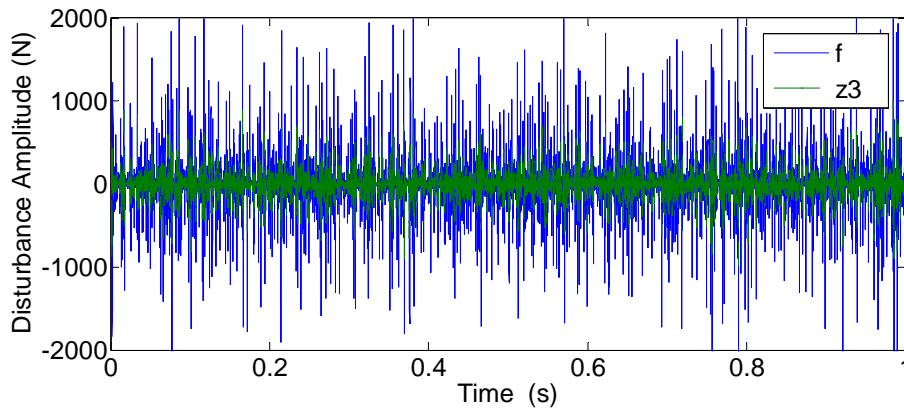
Figure 49: ESO tracking with increased bandwidths (wo=50000, wc=10000)

The effects of lowering the bandwidths have also been examined. The following figures show the closed loop performance and ESO tracking with significantly decreased bandwidths: wo=1000 and wc=5000. Even though the effect of noise is much smaller with lowered bandwidths, the ESO tracking (Figure 51) seems to suffer as a direct result. However, the overall closed loop performance (Figure 50) gives rise to even lower rotor vibration amplitudes.
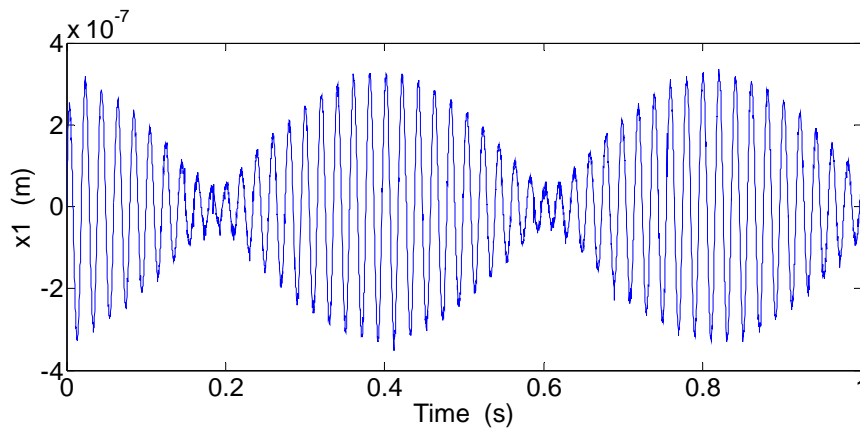
Figure 50: Closed-loop rotor vibration with sensor noise (wo=5000, wc=1000)
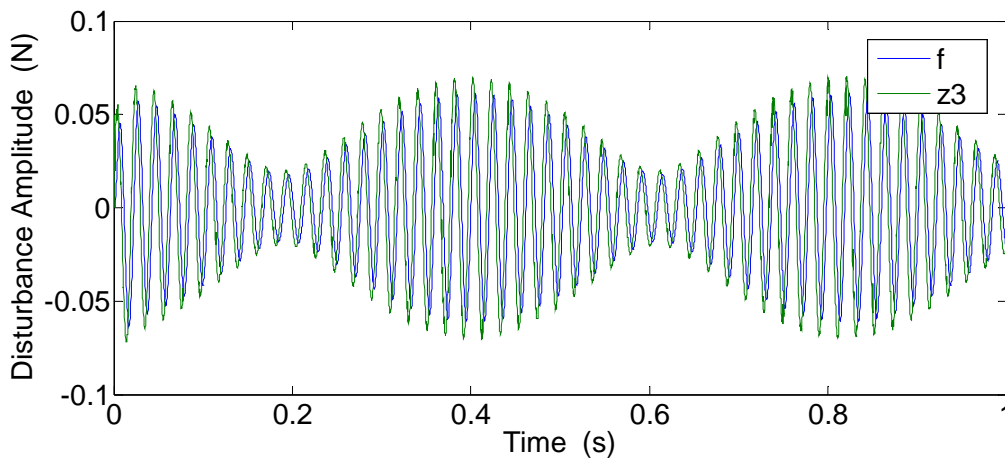
Figure 51: ESO tracking with lowered bandwidths (wo=1000, wc=200)

In summary, the effects of increase or decrease in controller and ESO bandwidths are complex in the presence of noise. A decrease seems to lead to good overall closed loop performance, but this would also sacrifice the ESO accuracy, which affects fault detection performance.

CHAPTER VI

AN EXPLORATION OF PID-INSPIRED NONLINEAR CONTROL

Active Disturbance Rejection Control, as developed and parameterized by Gao, is a linear control method. It has inherited the ease of use and simplicity of the popular PID controller, which is also a linear controller. Nonlinear methods for rotor vibration control exist, but many of them require complicated design setup. This is due to the complexity of the control laws used in most nonlinear control. For instance, an implementation of fuzzy logic control for rotor vibration reduction requires the setup of a number of inference rules for the synthesis of the control law. These rules are often to be based on the intuition of the designer, extensive prior knowledge of the plant, and more often than not, necessitate a fair amount of trial-and-error.

Controller complexity and the accompanying effect of tuning effort is an inherent issue in modern control design, as more and more control techniques developed in academia have moved in the direction of increasing controller complexity. A fundamental theme of this dissertation is to show that easy to use controllers such as ADRC can be designed and implemented to achieve high performance. In this chapter, a nonlinear controller developed by Han [43, 44] is applied to rotor vibration reduction. The Han Nonlinear PID (NPID) is a natural extension of the popular PID paradigm and has retained the precursor's simplicity and ease of use. In terms of tracking, the NPID has been shown to rival the performance of ADRC [45]. However, in terms of disturbance rejection and robustness, NPID is weaker.

6.1   Han's Nonlinear Controller

It has long been observed in industry that modifications of the PID (such as gain-scheduling) can improve the performance of the linear PID. But most solutions have been implemented on particular problems only and thus are not easily extended to a wider class of problems. The nonlinear PID proposed by Han was systematically developed based on a new analysis of the traditional PID controller, whose control law is given by

$$u_{PID} = k_P e + k_D \dot{e} + k_I \int e \, dt \,, \tag{6.1}$$

where e represents the error signal. The controller only has three tuning parameters and is linear. The first term acts proportionally to the value of the error, the second term is sensitive only to changes in the error and thus helps to improve the transient behavior. The last term makes the controller sensitive to small errors as they accumulate over time.

81

It is this integral term that makes the controller effective against steady state error, especially if a constant disturbance is present. However, the integral term often causes saturations in the controller (integral wind-up) and phase lag, which can make the controller unstable. As a result, the integral term is not often used in practice. A common solution found in industry, however, stipulates that the integral term should be canceled during transient response of the system. Such a design modification makes the controller effectively nonlinear. But it was not until recently that such modifications have been systematically documented and generalized, such as in the works of Han and Gao [43, 44, 45].

Han's nonlinear controller mimics the action of the integral term through a nonlinear modification, while avoiding the integral wind-up. The following control law is proposed:

$$u = k \left| e \right|^a sign(e), \quad \textit{for 0<a<1} \tag{6.2}$$

where the *sign(e)* represents the signum function. Its value is equal to 1 if the argument is positive, and -1 if the argument is zero or negative. Because the exponent *a* is between zero and unity, the term $\left| e \right|^a$ will be large if the error is small. This makes the controller more sensitive to small errors, which imitates the effect of the integral term.

It is interesting to note that if the exponent *a* of (6.2) is reduced to unity, the resulting control law is the proportional error law, which is represented by the first term of the PID. It has been shown in simulation [45] that for a second order linear system, steady-

state error, transient behavior and disturbance rejection improve with decreasing values of the exponent. In fact, if the exponent is zero, bang-bang control results:

$$u = k \cdot sign(e) \tag{6.3}$$

The bang-bang control is impractical because the control output vacillates between $+k$ and $-k$, causing excessive chattering. In a real system, such behavior could have deleterious effects on the actuator. The control signal becomes steadier with increasing values of a. Hence, there is a tradeoff between performance and steadiness of control signal. A comprise can be reached if the exponent is chosen to have a middle value, such as 0.5. With this choice, equation (6.2) becomes

$$u = k\sqrt{|e|}sign(e) \tag{6.4}$$

More recently, it has been pointed out that the control law given by (6.2) can be further improved for noise sensitivity, if the gain is limited to a linear control law if the errors are very small. This is because the high gain is maintained through the entire frequency spectrum, thus making the controller more susceptible to noise. A piecewise defined control law has been proposed.

$$u = k \cdot fal(e), \tag{6.5}$$

where the *fal*-function is defined as

$$fal(e) = k|e|^a sign(e), \quad \text{if } |e| > d \tag{6.6}$$

$$fal(e) = e/d^{1-a}, \quad \text{if } |e| \le d \tag{6.7}$$

This effectively limits the gain of the nonlinear controller to k/d^{1-a} in the neighborhood of d. It is interesting to compare the control law given by (6.5) to a proportional control law. Both laws are superimposed in Figure 30.

Alternatively, in order to reduce the sensitivity of the controller to noise, we can use an observer. Most applications in industry have used observers or filters in conjunction with the PID controller.
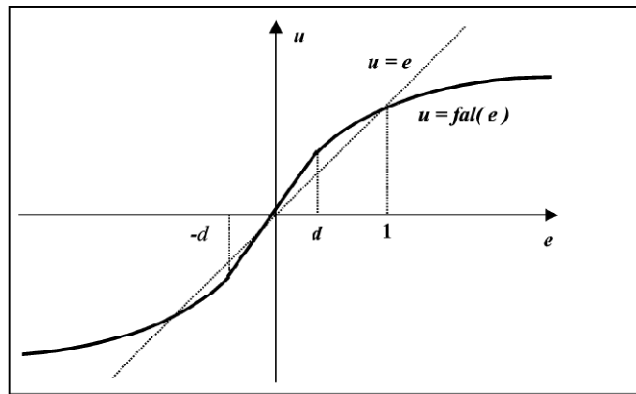
Figure 52: Linear vs. Han's nonlinear proportional control

Figure 30 shows certain interesting features that Han's nonlinear control shares with other more complex nonlinear controllers. When the error is small, the gain of Han's controller is larger than that of proportional control. As the error approaches unity, the gains of both controllers converge. At large errors, the gain of Han's controller actually becomes less susceptible to error than the proportional controller. As a matter of fact, many nonlinear control techniques, in particular, fuzzy logic control mentioned earlier, exhibit the same kind of behavior [45]. However, Han's controller is much easier to implement and to tune, and like the PID, it is not model dependent, which means that no

prior knowledge of the plant is required. In this aspect, this fact gives Han's controller a definitive advantage.

6.2   Construction of the Nonlinear Controller

The version of the nonlinear controller used in this study is similar to Han's originally proposed control law. It contains both a proportional and a derivative part.

$$u = k_P \sqrt{|e|} \, sign(e) + k_D \sqrt{|\dot{e}|} \, sign(\dot{e}) \tag{6.8}$$

The first term of (6.8) is the proportional term which is exactly the same as equation(6.4). The second term is an extension of the derivative term of the traditional PID controller, which provides additional performance for the transient response. As mentioned before, the integral part of the PID is mimicked by the nonlinear nature of the control law.

The Matlab Simulink implementation of the nonlinear controller given by equation (6.8) is shown in the following two figures. Figure 53 shows the high-level block diagram of equation (6.8), where the blocks g(e) and g(e)1 represent the function $g(e) = \sqrt{|e|} \, sign(e)$.
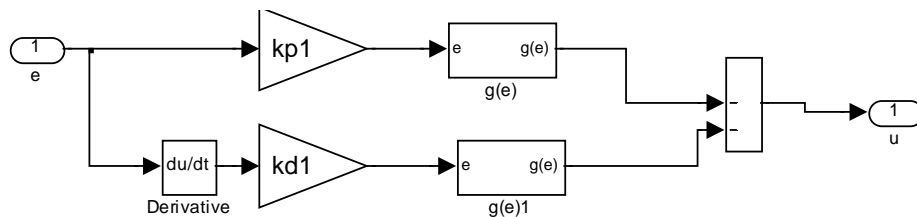
Figure 53: Simulink block diagram of the nonlinear controller of equation (6.8)

The details of the blocks which contain the function g(e) are shown in Figure 54. The block with the name "sign" represents the signum function.
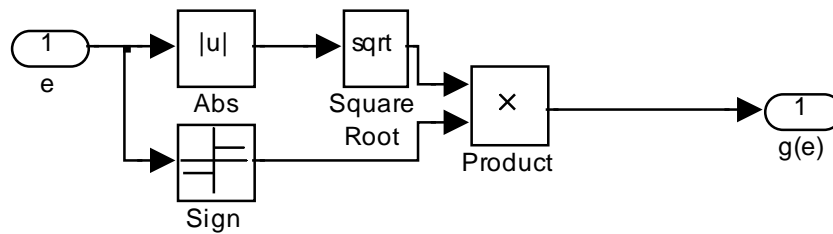
Figure 54: Block diagram of function g(e) of Figure 53

In the following, the simulation results of Han's nonlinear controller, in the form of equation (6.8), will be compared to that of the traditional proportional derivative controller. The two controllers share a high degree of similarity; both of them have two tuning parameters, the proportional and derivative gains, which have similar physical means. However, the nonlinear nature of Han's controller gives rise to some interesting phenomena in the rotor vibration reduction problem. Based on these observations, the effectiveness and practicality of the Han's nonlinear controller will be discussed.

6.3   Matlab Simulation

The nonlinear control is applied to the rotor vibration reduction problem. The simulation is carried out under a sinusoidal disturbance of 300 rad/s. Both controllers are tuned with Gao's parameterization technique, and thus the same gains are obtained for both

controllers. The proportional gain is kp=$(1000)^2$, and the derivative gain is kd=2×(1000).

Both controllers significantly reduce the amplitude of rotor vibration. Compared to the open-loop amplitudes, the reduction is five orders in magnitude. Both controllers also give rise to steady, periodic behavior. The results of the PD controller are shown in Figure 55 and Figure 56.
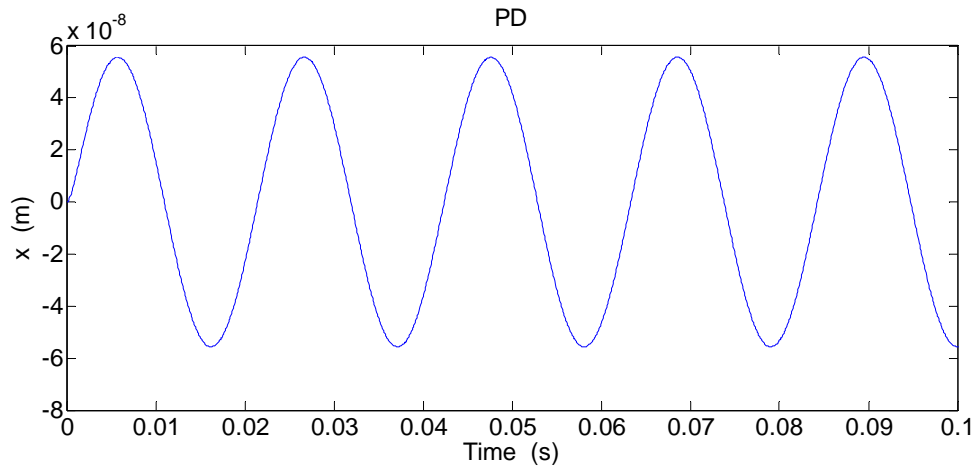
Figure 55: Rotor vibration reduction with traditional PD controller

The PD controller gives rise to a circular orbit of the rotor, as shown in Figure 55. Moreover, the control output, as shown in Figure 56, is a near-perfect sinusoid. The control effort varies between 0.9N and -0.9N, and the rotor deviation from the center is 6 ×10^{-8}m. These results are comparable to the ones obtained in the preceding chapters with linear controllers.

6.4   Distinctive Features of Nonlinear Control Results

The results of the nonlinear control are shown in Figure 57 and Figure 58. The rotor deviation amplitude is 3.7×10^{-8}m, slightly less than that achieved with the linear controller. The nonlinear control effort has an amplitude of 0.9N, which is the same as with the linear controller.
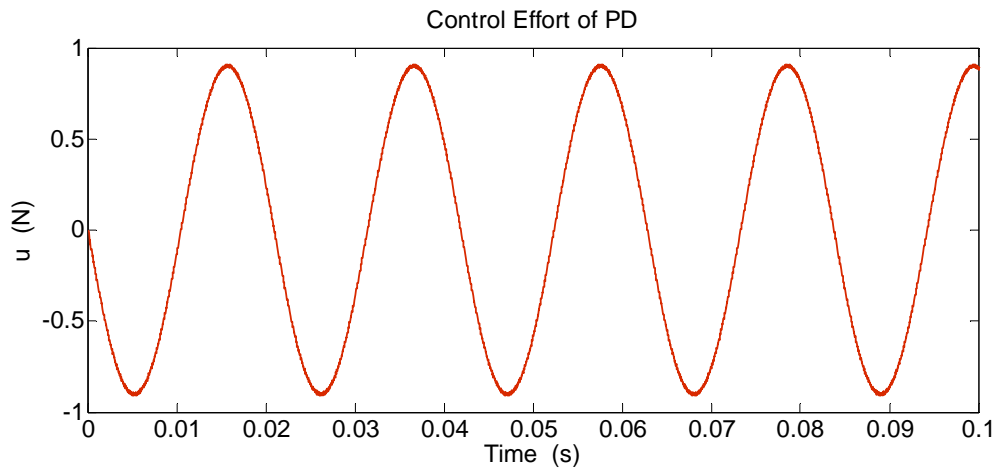
Figure 56: Control effort of the traditional PD controller

However, the nonlinear control exhibits qualitative differences in terms of the rotor orbit as well as the control output. As can been seen from Figure 57, the rotor orbit deviates from perfect circularity, even though it is still periodical. The presence of the distorted orbit is in itself not a problem. As long as the rotor deviations are within acceptable amplitudes, the exact nature of the rotor orbit is not an important factor when considering the performance of the controller.
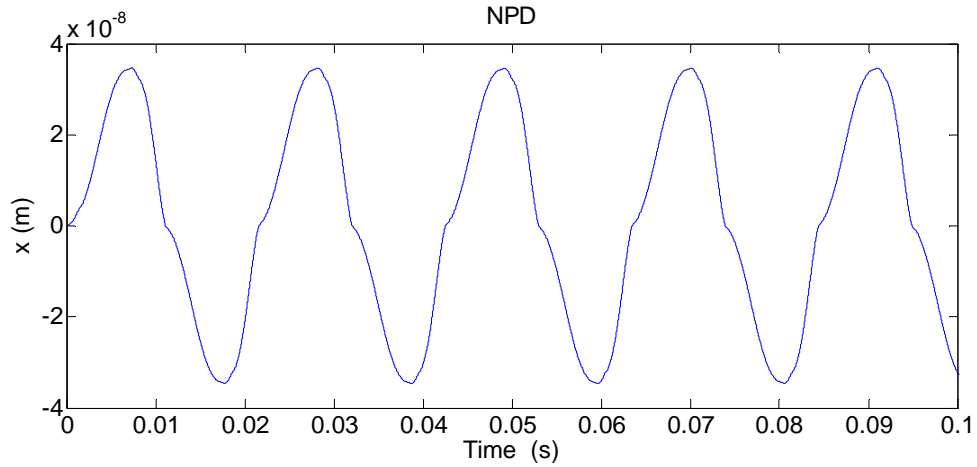
Figure 57: Rotor vibration reduction with Han's nonlinear controller

6.5 Sigmoidal Nonlinear Control

The signum function is non-continuous and may cause undesirable jitters. To deal with this particular problem, alternative functions have been proposed that mimic the signum function but are continuous throughout. The saturation function and sigmoid function are both viable alternatives. In particular, the sigmoid function is defined as follows.

$$
\begin{aligned}
sig(z) \quad &= -1 && \text{if } z < -1 \\
&= -0.5(2z+3)(3z+1) \,/\, (4z2+6z+1) && \text{if } -1 < z < -0.5 \\
&= -0.5z(2z+3) \,/\, (4z2+2z-1) && \text{if } -0.5 < z < 0 \\
&= 0.5z(2z-3)/ \,(4z2-2z-1) && \text{if } 0 < z < 0.5 && (6.9) \\
&= 0.5(2z-3)(3z-1) \,/\, (4z2-6z+1) && \text{if } 0.5 < z < 1 \\
&= 1 && \text{if } z > 1
\end{aligned}
$$
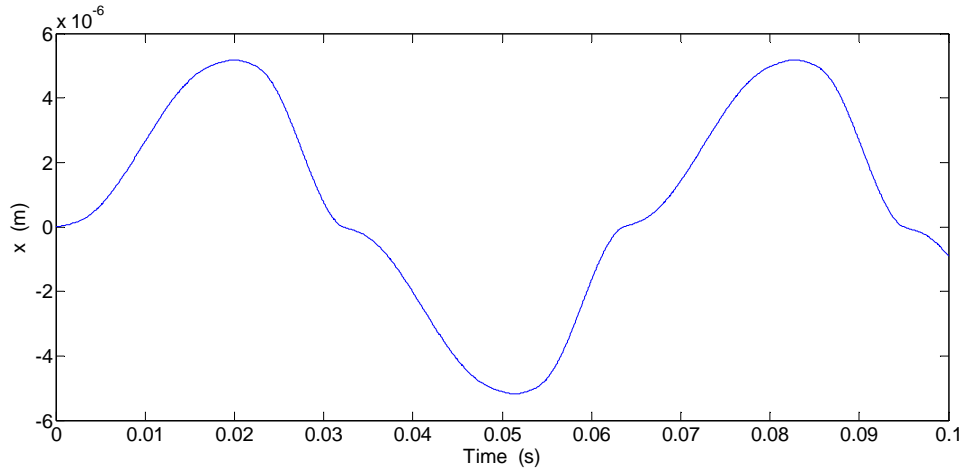
Figure 58: Rotor vibration control with sigmoidal nonlinearity (w=100)
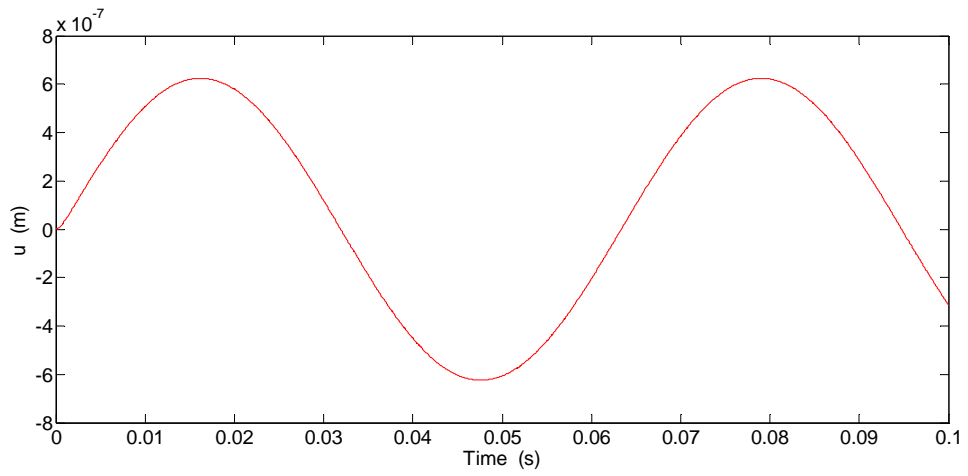
Figure 59: Control effort with sigmoidal nonlinearity (w=100)

CHAPTER VII

CONCLUDING REMARKS

7.1 *Summary of the Work*

In a set of projects, the novel Active Disturbance Rejection Control (ADRC) has been applied to various problems involving flywheel rotor operation. These applications include rotor levitation, steady state rotation and accelerating operation. Several models such as the mass point model and distributed three-mass models have been analyzed. In each of these applications, the ADRC has been extended to cope with disturbance, noise, and control effort optimization; it also has been compared to various industry-standard controllers such as PID and PD/observer, and has proved to be superior. The control performance of the PID controller and the PD/observer currently used at NASA Glenn has been improved by as much as an order of magnitude. For the sake of summary, the main results of the comparisons have been tabulated below.

Table 1: Controller comparison for flywheel rotor levitation

	Settling Time (s)	Steady State Error (mm)	Min/ Max Control Effort (N)	Disturbance Peak Amplitude (mm)	Disturbance Recovery Time (s)
PD/Observer	0.32	0.01	-0.05/0.05	0.14	NA
PID	0.38	0	-0.05/0.05	0.06	0.09
ADRC	0.31	0	-0.05/0.05	0.01	0.01

Table 2: Controller comparison for accelerating operation (point-mass model)

	Vibration Amplitude (m) at t = 5s	Vibration Amplitude (m) at steady state	Max. Control Effort (N) at t = 5s	Max. Control Effort (N) at steady state
Open loop	1.1×10^{-3}	1.0×10^{-3}	NA	NA
PD/Observer	0.9×10^{-5}	4.5×10^{-5}	0.3×10^{4}	1.05×10^{4}
ADRC	0.4×10^{-6}	3.3×10^{-6}	0.3×10^{4}	1×10^{4}

Table 3: Controller comparison for accelerating operation (distributed-mass model)

	X1 Vibration Amplitude (m)	X2 Vibration Amplitude (m)	X3 Vibration Amplitude (m)	U1 Max. Control Effort (N)	U2 Max. Control Effort (N)	U3 Max. Control Effort (N)
Open loop	0.005	0.008	0.005	NA	NA	NA
PID	0.9×10^{-7}	3×10^{-6}	0.9×10^{-7}	9.5	300	9.5
ADRC	0.2×10^{-7}	2×10^{-6}	0.2×10^{-7}	3	300	3

7.2   *Discussion of the Results*

Throughout these projects, particular attention has been paid to the tuning of the designed control systems. It has been emphasized that simplicity and ease of tuning is an industrial objective that must not be disregarded in the control design. The ADRC has inherited the simplicity of the PID controller and has decreased the number of tuning parameters effectively to one. This simplification has additional advantages in implementation. For instance, a considerable amount of time was spent on tuning the PID for the distributed mass rotor-shaft system, whereas little effort was necessary for tuning the ADRC.

Along the same line of thought, a nonlinear controller, which is an intuitive extension of the PID, has been considered. Even though Han's nonlinear PD controller exhibits similar ease of use and is comparable in performance, although it causes the rotor orbit to deviate from circularity. Since nonlinear controllers PD controllers can be combined with the ESO, such approach offers additional improvement in control performance. One promising application is the nonlinear ADRC control of the MEMS gyroscope. The similarity between rotor vibration control and the MEMS gyroscope control is striking, and preliminary results indicate that nonlinear control may improve existing ADRC control of MEMS gyroscopes.

Another innovation of this research is the control application of the disturbed mass model. Even though this model is well known in vibration analysis, it has not been widely used in vibration control, where the Jeffcott rotor is the dominant approach. The

complexity of the Jeffcott model is considerable when analyzing accelerating motion. Control researchers seldom deal with accelerating operations, often citing the complexity of the rotor model. The distributed mass model, however, is very suitable for vibration control studies. The control of accelerating rotor motion can be straightforwardly addressed using this approach. Finally, it may be noted that the Jeffcott rotor is most applicable for modeling disk-shaped rotors. The rotor described in the distributed mass model is a cylinder, which is more common rotor shape in practice.

REFERENCES

[1] Kenny, B.H., Kascak, P.E., Jansen, R., Dever, T., Santiago, W, "Control of a High Speed Flywheel System for Energy Storage in Space Applications," IEEE Transactions on Industry Applications, Volume 41, No. 4, pp. 1029-1038, 2005.

[2] Childs, D., "Turbomachinery Rotordynamics," John Wiley & Sons, New York, 1993.

[3] Patel, M., "Spacecraft Power Systems," CRC Press, 2004.

[4] Dever, P., Brown, G., and Jansen, P., "Estimator Based Controller for High Speed Flywheel Magnetic Bearing System," NASA Internal Report (NASA/TM-2002-211795), 2002.

[5] Minorsky, N., "Directional Stability and Automatically Steered Bodies," J. Am. Soc. Nav. Eng., Volume 34, No. 2, pp. 280-309, 1922.

[6] Cunningham, R. E., "Steady-State Unbalance Response of a Three-Disk Flexible Rotor on Flexible, Damped Supports," Journal of Mechanical Design, Volume 100, pp. 563-73, 1978.

[7] Nikolajsen, J.L., and Holmes, R., "Investigations of Squeeze-film Isolators for the Vibration Control of a Flexible Rotor," Journal of Mechanical Engineering Science, Volume 21, pp. 247-52, 1979.

[8] Ashour, O., and Rogers, C., "Magnetorheological Fluids: Materials, Characterization, and Devices," Proc. 6th Int. Conf. on Adaptive Structures, pp. 23-34, 1995.

[9] Siebert, M., "A Passive Magnetic Bearing Flywheel," NASA Internal Report" (NASA/TM-2002-211159), 2002.

[10] Dyer, S.W., and Ni, J., 1999, "Adaptive Influence-Coefficient Control of Single-Plane Active Balancing Systems," Proceedings of the ASME International Mechanical Engineering Conference and Exposition, Volume 10, pp. 747-55, 1999.

[11] Van de Vegte, J., and Lake, R. T., "Balancing of Rotating Systems During Operation," Journal of Sound and Vibration, Volume 57, pp. 225-35, 1978.

[12] Van De Vegte, J., "Balancing of Flexible Rotors During Operation," Journal of Mechanical Engineering Science, Volume 23, pp. 257-61, 1981.

[13] Van De Vegte, J., "Continuous Automatic Balancing of Rotating Systems," Journal of Mechanical Engineering Science, Volume 6, pp. 264-69, 1964.

[14] Bishop, R.E.D., "On the Possibility of Balancing Rotating Flexible Shafts," Journal of Mechanical Engineering Science, Volume 24, pp. 215-220, 1982.

[15] Halliday, D., "Fundamentals of Physics," Wiley and Sons, New York, 2007.

[16] Hagwood, N.W., Chung, W.H. and Von Flowtow, A. "Modeling of Piezoelectric Actuator Dynamics for Active Structural Control," Journal of Intelligent Material Systems and Structure, Volume 1, pp. 327-35, 1990.

[17] Maguerre, "Mechanics of Vibration," Sijthoff & Nordhoff, 1994.

[18] Barret, T. S., Palazzolo, A.B., and Kascak, A. F., "Active Vibration Control of Rotating Machinery Using Piezoelectric Actuators Incorporating Flexible Casing Effects," Journal of Engineering for Gas Turbines and Power, Volume 117, pp. 176-87, 1995.

[19] Tang, P., Palazzolo, A., Kascak, A., Montague, G., and Li, W., "Combined Piezoelectric-Hydraulic Actuator Based Active Vibration Control for Rotordynamic Systems," Journal of Vibration and Acoustics, Volume 117, pp. 285-293, 1995.

[20]   Horst, "Aktive Schwingungsminderung mit piezoelektrischen Aktuatoren an einer elastischen Balkenstruktur," Schwingungen in Anlagen und Maschinen, VDI Verlag GmbH, Duesseldorf, 2001.

[21]   Gasch, "Rotordynamik," Springer Verlag, Berlin-Heidelberg, 2002.

[22]   Kraemer, "Dynamics of Rotors and Foundations," Springer Verlag, Berlin-Heidelberg, 1993.

[23]   Dorf, "Modern Control Systems," 10th Edition, Prentice Hall, 2004.

[24]   Schweitzer G., Bleuler, H., and Taxler, A., "Active Magnetic Bearings," vdf Hochschulverlag AG and ETH, Zurich, 1993.

[25]   Kucera, L., "Robustness of Self-Sensing Magnetic Bearing" Proceedings of the Magnetic Bearings Industrial Conference, pp. 261-270, 1997.

[26]   Nise, "Control Systems Engineering, 4th Edition," *Addison and Wiley*, 2003.

[27]   Alexander, "Fundamentals of Electric Circuits," 2nd Edition, *McGraw-Hill*, 2004.

[28]   Duan, G. R., Wu Z. Y., Bingham C., and Howe D., "Robust Control of a Magnetic-Bearing Flywheel Using Dynamical Compensators," Transactions of the Institute of Measurement and Control, Volume 23, pp. 249-278, 2001.

[29]   Shen, J. Y., Fabien, B.C., "Optimal Control of a Flywheel Energy Storage System with a Radial Flux Hybrid Magnetic Bearing," Journal of the Franklin Institute, Volume 339, pp. 198-210, 2002.

[30]   Stienmier, J.D., Thielman, S.C., and Fabien, B.C., "Flywheel Energy Storage System with a Hybrid Magnetic Bearing," Trans. ASME, Volume 119, pp. 650-656, 1997.

[31]   Hubbard, M., and McDonald, P., "Feedback Control Systems for Flywheel Radial Instabilities," Flywheel Technology Symposium Proceedings, pp.209-217, 1980.

[32]   Stanway, R., and O'Reilly, J., "State Variable Feedback Control of Rotor Bearing Suspension Systems," Proceedings of the Third International Conference on Vibrations in Rotating Machinery, pp. 515-524, 1984.

[33]   Sinha, A., Meese, K. L., and Wang, K. W., "Sliding Mode Control of a Rigid Rotor via Magnetic Bearings," ASME Biennial Conference on Mechanical Vibration and Noise, Miami, Florida, 1991.

[34]   Salm, J. R. and Schweitzer, G., "Modeling and Control of a Flexible Rotor with Magnetic Bearings," Proceedings of the Third International Conference on Vibrations in Rotating Machinery, 1984.

[35]   Matsumura, F., and Yoshimoto, T., "System Modeling and Control Design of a Horizontal-shaft Magnetic Bearing System," IEEE Transactions on Magnetics. Volume 22, pp. 196-203, 1995.

[36]   Hung, J. Y., "Magnetic Bearing Control Using Fuzzy Logic," IEEE Transactions on Industry Applications, Volume 31, pp. 1492-1497, 1996.

[37]   Gao, Z., "Scaling and Parameterization Based Controller Tuning," Proceedings of the 2003 American Control Conference, pp. 4989-4996, 2003.

[38]   Han, J., "A Class of Extended State Observers for Uncertain Systems," Control and Decision, Volume 10, No.1, pp. 85-88, 1995.

[39]   Bay, S., "Fundamentals of Linear State Space Systems," International Edition, McGraw-Hill, 1999.

[40]   Wauer, J., "On the Dynamics of Cracked Rotors: A Literature Survey," Applied Mechanics Review, Volume 43, pp. 13-17, 1990.

[41]   Dimarogonas, A.D., "Vibration of Cracked Structures: A State of Art Review," Engineering Fracture Mechanics, Volume 55, pp. 831-857, 1996.

[42]   Radke, A., "On Disturbance Estimation and its Applications in Health Monitoring," Cleveland State University Dissertations, 2006.

[43]   Han, J., "Control Theory: Is it a Theory of Model or Control?", Systems Science and Mathematical Sciences, Volume 9, No. 4, pp. 328-335, 1989.

[44]   Han, J., "Nonlinear Tracking Differentiator," Systems Science and Mathematical Sciences, Volume 14, No. 2, pp. 177-183, 1994.

[45]   Gao, Z., "An Alternative Paradigm for Control System Design," Proceedings of the 40th IEEE Conference on Decision and Control, pp. 4578-4585, 2001.